An Experimental and Numerical Investigation of Homogeneous Ignition in Catalytically Stabilized Combustion of Hydrogen/Air Mixtures Over Platinum

CHRISTOPH APPEL, JOHN MANTZARAS,* ROLF SCHAEREN, ROLF BOMBACH, ANDREAS INAUEN, BEAT KAEPPELI, BERND HEMMERLING, and ANNA STAMPANONI

Paul Scherrer Institute, Combustion Research, CH-5232, Villigen PSI, Switzerland

The gas-phase ignition of fuel-lean hydrogen/air mixtures over platinum was investigated experimentally and numerically in laminar channel-flow configurations. Experiments were performed at atmospheric pressure in an optically accessible catalytic channel combustor established by two Pt-coated parallel plates, 300 mm long (streamwise direction) and placed 7 mm apart (transverse direction). Planar laser induced fluorescence (PLIF) of the OH radical along the streamwise plane of symmetry was used to monitor the onset of homogeneous ignition, one-dimensional Raman measurements (across the 7-mm transverse direction) provided the boundary layer profiles of the major species and temperature, and thermocouples embedded beneath the catalyst yielded the surface temperature distribution. Computations were carried out using a two-dimensional elliptic fluid mechanical model that included multicomponent transport and elementary homogeneous (gas-phase) and heterogeneous (catalytic) chemical reaction schemes. Four homogeneous and three heterogeneous reaction schemes were tested in the model against measured homogeneous ignition characteristics. The differences between measured and predicted homogeneous ignition distances could be substantial (ranging from 8% to 66%, depending on the particular hetero/homogeneous schemes) and were ascribed primarily to the homogeneous reaction pathway. Sensitivity analysis indicated that the discrepancies induced by the gas-phase schemes originated either from the presence of heterogeneously-produced water due to its effectiveness as collision partner in the chain terminating reaction $H + O_2 + M = HO_2 + M$, or from an overall overprediction of the radical pool in the preignition zone. The heterogeneous schemes had significant differences in their surface coverage and radical fluxes, but these variations had practically no impact on homogeneous ignition. Sensitivity and reaction flux analyses have shown that this was attributed to the ability of all heterogeneous schemes to capture the measured mass-transport-limited fuel conversion and to the relative insensitivity of homogeneous ignition on the magnitude of the heterogeneous radical fluxes, provided that all radical adsorption reactions (OH, H, and O) were included in the heterogeneous schemes.

NOMENCLATURE

b	Channel half-height, Fig. 1
c_p	Specific heat at constant pressure
C_k	Concentration of gas-phase species
D_{kl}	Multicomponent diffusion coefficient, Eq. 7
D_k^T	Species thermal diffusion coefficient, Eq. 7
D_{km}	Mixture-average species diffusion coefficient, Eq. 8
D_k	Effective species diffusion coefficient, Eq. 12
E	Activation energy
h	Total enthalpy, Eq. 4
h_k^o	Chemical enthalpy of gas-phase species, Eq. 9
J_k	Heterogeneous molar flux of gas-phase species
k	Reaction rate coefficient
K_c	Reaction equilibrium constant
K_g	Total number of gas-phase species
M_s	Total number of surface species
L	Channel length, Fig. 1
Le	Lewis number (thermal over species diffusivity)
n	Sum of surface reactants' stoichiometric coefficients, Eq. 14
p	Pressure
R	Universal gas constant
$\dot{s}_k$	Species heterogeneous molar production rates, Eqs. 6 and 10
T	Temperature
T_o	Reference temperature, Eq. 9
u	Streamwise velocity
U_{IN}	Inlet streamwise velocity

* Corresponding author. E-mail: ioannis.mantzaras@psi.ch

0010-2180/02/$–see front matter
PII S0010-2180(01)00363-7

COMBUSTION AND FLAME 128:340–368 (2002)

Published by Elsevier Science Inc.

v	Transverse velocity
$\bar{V}_k$	Species diffusion velocity vector, Eq. 7
$\dot{w}_k$	Gas-phase species molar production rate, Eq. 5
W	Channel width, Fig. 1
W_k	Gas-phase species molecular weight
$\bar{W}$	Average gaseous mixture molecular weight
x	Streamwise physical coordinate
X_k	Gas-phase species mole fraction
y	Transverse physical coordinate
Y_k	Gas-phase species mass fraction
z	Lateral physical coordinate

Greek Symbols

γ_k	Sticking coefficient of gas-phase species, Eq. 14
Γ	Surface site density, Eq. 6
$\theta_{T,k}$	Species thermal diffusion ratio, Eq. 8
Θ_m	Surface species coverage, Eq. 6
λ	Thermal conductivity of the gas
λ_s	Thermal conductivity of the solid
μ	Viscosity
ρ	Density
σ_m	Surface species site occupancy, Eq. 6
τ	Flow residence time, Eq. 13
φ	Equivalence ratio
$\omega_i(A)$	Third body efficiency of gaseous species A in reaction i

Subscripts

ads, des	Adsorption, desorption
ig	Ignition
IN	Inlet
k, m	Index for gas-phase species, index for surface species
W	Wall
x, y	Streamwise and transverse components

INTRODUCTION

Catalytically stabilized combustion (CST) is an efficient and cost-competitive combustion technology for low NO_x emissions and has been recently introduced to gas turbines of power generation systems [1, 2]. Today, gas turbine emission regulations require NO_x levels of 3 to 25 ppm, the lower end of the range currently enforced in severe non-attainment areas in the U.S.A. (3 ppm) and in the most stringently regulated areas in Japan and Europe (5 ppm). Forthcoming emission legislation for ozone and particulate matter will also impact gas turbines since NO_x is involved in the formation of both pollutants; the trend for NO_x emissions will, therefore, shift toward the lower end of their allowable range. Small-scale gas turbines (~1.5 MW) refitted with catalytic combustors have demonstrated NO_x emissions less than 3 ppm [2] and current efforts intensify on large-scale (>150 MW) machines [3]. In the adopted hybrid CST approach [1, 2] about half of the fuel is converted catalytically, stabilizing with thermal and chemical interactions a subsequent gas-phase combustion zone.

Further improvement in CST technology requires the development of catalysts with enhanced activity and thermal stability, understanding of the fundamental surface processes including catalyst-substrate interactions, knowledge of low-temperature homogeneous (gas-phase) kinetics and their coupling with the corresponding heterogeneous (catalytic) kinetics. Moreover, the combustor geometry (large surface-to-volume ratio catalytically coated channels) calls for the development of multidimensional numerical tools with capabilities of detailed hetero/homogeneous chemistry, transport, and flow description. Heterogeneous kinetic studies of simple fuels such as H_2, CO, and CH_4 over Pt or Pd have progressed significantly over the last years [4–10] and multidimensional models incorporating detailed surface and gas-phase kinetics are now available [11–13]. In the latter group of studies we investigated numerically [11] and experimentally [12] the homogeneous ignition of CH_4/air mixtures over Pt using a 2-D elliptic fluid mechanical model with elementary hetero/homogeneous reaction schemes and an optically accessible catalytic combustor with a well-defined 2-D channel geometry. Analytical homogeneous ignition criteria for channel-flow CST were further established [14] and applied to CH_4/air CST [15].

In power generation there is increased interest for hydrogen-assisted CST. Addition of small amounts of H_2 in natural gas can reduce the catalyst light-off temperature (and possibly eliminate the catalyst preburner [2]) and can

improve stability by damping combustion-induced pulsations. Hydrogen can be feasibly produced via partial catalytic oxidation of a small fraction of the fuel in an upstream reactor [16]. Hydrogen can be also part of the fuel, for example, synthesis gas, albeit power generation is then limited to areas near chemical plants. The detailed knowledge of hydrogen CST is an important step in the understanding of hydrogen-assisted CST. Of particular attention in hydrogen and hydrogen-assisted CST is the control of catalyst hot-spots and the potential of homogeneous ignition within the catalytic reactor: H_2 is a strongly diffusionally imbalanced fuel with a Lewis number of $\approx$0.3, leading to superadiabatic surface temperatures [17, 18] that endanger the catalyst integrity and, in addition, favor the onset of homogeneous ignition due to increased heat transfer towards the near-wall gas. Elementary heterogeneous reaction schemes for the oxidation of H_2 on platinum—the catalyst of interest in the present study—were developed mainly over the last 15 years [4–8], whereas corresponding homogeneous schemes [19–22] were a result of a longer development period. The hetero/homogeneous chemistry coupling and the homogeneous ignition of H_2/air over Pt were investigated numerically in the following studies, all of which included detailed gaseous chemistry: 1-D stagnation point flows were investigated by Ikeda et al. [23] with simplified surface chemistry and by Bui et al. [18] with detailed surface chemistry, flat plate flows were examined in Schefer [24] and Markatou et al. [25] with 2-D parabolic models and simplified surface chemistry, and channel flows were studied in Buser et al. [26] with a 2-D elliptic model and simplified surface chemistry. The effect of turbulence, relevant under the high-pressure operation of power systems, was investigated recently [27] in H_2/air CST with a 2-D elliptic model and detailed hetero/homogeneous reaction schemes. Finally, Deutschmann et al. [28] studied numerically and experimentally the purely heterogeneous aspects of hydrogen-assisted CH_4/air CST; they used a 2-D elliptic model with detailed heterogeneous kinetics to simulate light-off characteristics in a monolithic channel configuration. Homogeneous ignition of H_2 air mixtures in 2-D configurations relevant to CST and, in particular, the ability of various hetero/homogeneous reaction schemes to correctly predict measured homogeneous ignition characteristics has not been reported in the literature.

In this article we undertake an experimental and numerical investigation of H_2/air CST over Pt in laminar channel flows. Experiments have been performed in an optically accessible catalytic channel combustor formed by two Pt-coated parallel ceramic plates, locally cooled to suppress hot-spot formation. Planar laser induced fluorescence (PLIF) of the OH radical along the streamwise plane of symmetry monitored the onset of homogeneous ignition, 1-D Raman (across the channel transverse direction) provided the boundary layer profiles of the major species and temperature, and thermocouples embedded beneath the catalyst surfaces yielded the catalyst temperature distribution along the streamwise direction. Numerical computations were carried out with a 2-D elliptic flow model that included multicomponent transport and detailed hetero/homogeneous chemistry description. Four well known homogeneous and three heterogeneous schemes were tested in the numerical model against measured homogeneous ignition characteristics, with main objective to validate their applicability in CST. A particular objective was to identify via sensitivity and reaction path analyses the origin of the differences among the various schemes.

First the burner configuration, the experimental conditions and the measuring techniques are introduced and then the numerical model, the solution algorithm, and the employed hetero/homogeneous chemical schemes are presented. Comparisons between measurements and predictions follow, the validity of the different homogeneous and heterogeneous schemes is assessed, sensitivity and reaction path analyses elucidate the differences among the various reaction schemes and finally the structure of the resulting flames and the CST applicability of a simpler (parabolic) numerical model are discussed.

EXPERIMENTAL

Burner Geometry and Flow Conditions

A catalytic burner especially suited for H_2/air CST has been built, using design concepts based

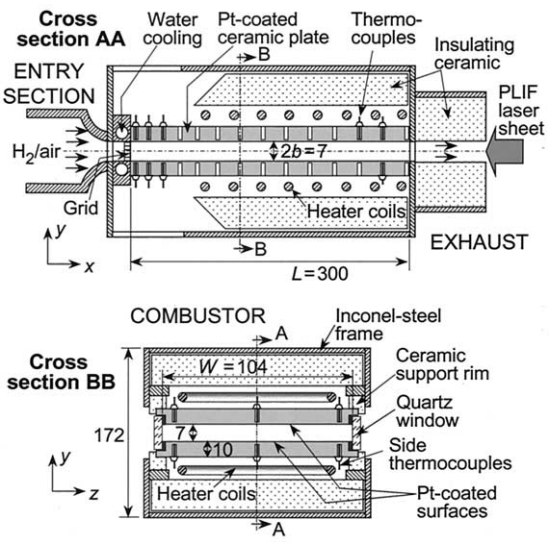

Fig. 1. Schematic of the catalytic combustor test rig. The reactor is defined by the volume $L \times W \times 2b$. All distances are in mm.

on our earlier, smaller-size CH_4/air reactor [12]. The combustor (see Fig. 1) consisted of two horizontal Si[SiC] ceramic plates, 300 mm long (L), 110-mm wide and 10-mm thick. Four rectangular ($4 \times 4 \times 7$ mm^3) ceramic spacers were positioned at the plate corners to maintain a constant plate separation of 7 mm ($2b$). Both Si[SiC] plates were bevelled at their edges to accommodate two quartz windows 300-mm long, 12-mm high, and 3-mm thick. The quartz windows were spring-pressed against the ceramic plates with 1-mm thick soft ceramic gaskets placed in between; the resulting lateral window separation was 104 mm (W). The channel combustor volume was delineated by the $300 \times 104 \times 7$ mm^3 enclosure (see Fig. 1). Optical accessibility was provided from both 300 mm $\times$ 7 mm sides, excluding two 18-mm long sections (near the center of each window) blocked by the window spring-support assemblies. The inner horizontal surfaces of the Si[SiC] plates were coated with platinum. Plasma vapor deposition (PVD) was used to apply a 1.5-μm thick nonporous Al_2O_3 layer followed by a 2.2-μm thick Pt layer. The resulting Pt surface distribution was very uniform and the adhesion of the Al_2O_3 and Pt layers was stable at the high catalyst temperatures (up to 1,250 K) of this study. Although direct PVD of Pt on Si[SiC] was possible, the Al_2O_3 served as a barrier to Pt-Si chemical interactions; such interactions are known in the literature and were also observed in the present work by X-ray photoelectron spectroscopy analysis. The surface temperature was monitored along the symmetry plane ($z = 0$) with 1-mm thick S-type thermocouples (14 for each plate) embedded 0.9 mm beneath the Pt-coated surfaces through 1.2 mm in diameter and 9.1-mm deep holes eroded from the outer plate sides. Given the high thermal conductivity of Si[SiC] (35 $Wm^{-1}K^{-1}$ at 1,300 K), the thermocouple measurements reflected closely the actual catalyst surface temperature. The spacing between successive thermocouples was finer at the entrance to resolve the steeper entry temperature gradients (the thermocouple locations are illustrated in the forthcoming Fig. 4). Additional thermocouples were positioned at side locations ($z = \pm 40$ mm, at $x = 22$ and 110 mm). All thermocouples were secured firmly in their holes with alumina cement. The channel reactor assembly was supported on ceramic rims that were, in turn, positioned inside an inconel-steel frame. To facilitate the Raman experiments, the test rig was mounted on an optical table traversable in the x-direction.

In the catalytic combustion of fuel-lean H_2 air mixtures, the catalyst can reach superadiabatic temperatures because of the low Lewis number of the deficient fuel: the surface equivalence ratio of H_2 is nearly twice that of the gas-phase [18]. The following computations demonstrate the experimental difficulties encountered in H_2/air CST. Figure 2 illustrates 2-D numerical predictions of the catalyst temperature distribution in the channel geometry of Fig. 1 (300 mm $\times$ 7 mm) with, typical for this study, inlet conditions of $U_{IN} = 2$ m/s, $T_{IN} = 310$ K, and $\varphi = 0.28$. Purely heterogeneous H_2/air combustion was considered with two different models: ideal adiabatic mass-transport-limited catalytic combustion and non-adiabatic catalytic combustion with the elementary heterogeneous scheme of hydrogen on Pt from Deutschmann et al. [5]. In the non-adiabatic case, radiation from the hot catalyst surfaces and 1-D axial heat conduction inside the solid plates were accounted for. The inlet and outlet temperatures in the radiation exchange model were taken as T_{IN} and $T_{e,m}$ (mean gas exit temperature), respectively. De-

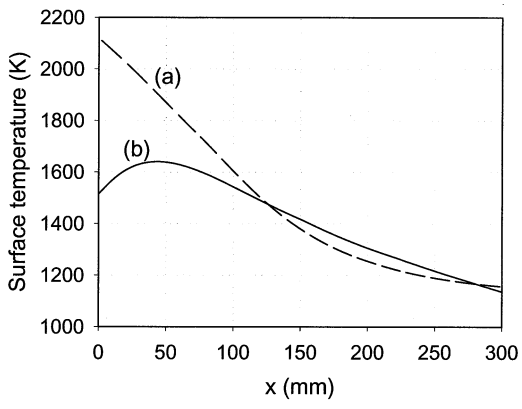

Fig. 2. Numerical predictions of the catalyst temperature distribution in H_2/air channel-flow catalytic combustion: U_{IN} = 2 m/s, T_{IN} = 310 K, φ = 0.28 and channel half-height b = 3.5 mm: (a) Adiabatic calculations with mass-transport-limited catalytic fuel conversion, (b) Non-adiabatic simulations with elementary heterogeneous reactions [5], surface radiation (with a surface emissivity of 0.6) and heat conduction (λ_s = 35 $Wm^{-1}K^{-1}$) in the solid substrate. Complete fuel conversion is attained at the channel exit in both cases. The adiabatic flame temperature is T_{af} = 1148 K. Superadiabatic temperatures are attained in both (a) and (b). In (a) the temperature at $x = 0$ approaches the theoretical flat plate limit $T = T_{IN} + (\Delta T_R)Le^{-2/3} \approx$ 2,100 K (with $\Delta T_R = T_{af} - T_{IN}$ and $Le \approx 0.32$). In (b) the rear section has higher temperatures than those of (a) because of heat conduction from the hotter entry.

tails of the non-adiabatic model can be found elsewhere [11]. As evidenced from Fig. 2, the temperature is highest at the entry, not only endangering the catalyst structural integrity but also compounding homogeneous ignition studies: experiments showed that, under non-adiabatic conditions similar to those of Fig. 2, the gaseous flame anchored directly at the hot entrance. To suppress the high catalyst entry temperatures and hence to control the onset of homogeneous ignition, the initial channel section had to be cooled more efficiently than simple thermal radiation allowed. Therefore, the 110 × 10 mm^2 entry sides of the ceramic plates were contacted to a water-cooled section of the inconel-steel frame (see Fig. 1); a 0.2-mm thick alumina cement was placed in between to maintain tight contact. In addition, the initial 60 mm of the outer ceramic plate surfaces were allowed to radiate to the cold environment by removing 80-mm long sections of the inconel-steel frame above (or below) the corresponding plate-sections. In the remaining 240 mm plate-length, heat was supplied by two independently-controlled 2.5 kW resistive heaters positioned 15 mm above the outer plate surfaces. The external heating was necessary to counteract heat losses; such losses should not be understated in the low flow-rate laminar experiments of this work. The absolute difference between top and bottom plate temperature distributions was, at any given axial location, less than 6 K. A 5-cm thick, porous, fiber ceramic insulation was placed between the heaters and the inconel-steel frame.

Air and hydrogen were supplied from an oil-free compressor and high-pressure bottles, respectively. The fuel and air flow rates were measured by two calibrated Brooks mass flow controllers; the accuracy in determining the mixture equivalence ratio was better than 2%. The reactants were mixed in two sequential Sulzer static mixers, passed through a section filled with 2-mm diameter metallic spheres to straighten the flow and, finally, were brought to the combustor through an entry section 400 × 21 × 104 mm^3 (in x-y-z) with an ending y-contraction ratio of 3:1. A 2-mm long metal grid (1 mm^2 mesh) was positioned on the water-cooled frame just upstream of the catalyst, to maintain uniform inlet temperature and velocity profiles. A retractable thermocouple monitored the inlet temperature after the grid. Finally, an inconel-steel exhaust-unit insulated with porous ceramic was placed downstream of the combustor. The open side of the exhaust allowed for additional optical access, through which the OH-PLIF laser sheet (see Fig. 1 and discussion in next section) was introduced into the combustor. Data acquisition and control was achieved by National Instruments hardware and software through a dedicated personal computer.

All experiments were performed at atmospheric pressure. The laminar experimental conditions are given in Table 1. The Reynolds numbers were based on the inlet properties and the channel hydraulic diameter (=13.1 mm); the actual Reynolds numbers inside the channel were lower than those of Table 1 because of the substantial mixture heating. The relatively low inlet temperatures reflected the efficient water-cooling of the entry section. Safety considerations determined the higher equivalence ratio

TABLE 1

Experimental Conditions[a]

Case	φ	U_{IN} (m/s)	T_{IN}(K)	Reynolds Number
1	0.28	1.6	313	1105
2	0.32	1.6	313	1092
3	0.28	2.0	312	1389
4	0.32	2.0	312	1371
5	0.28	3.0	312	2084
6	0.32	3.0	312	2057

[a] equivalence ratio, inlet velocity and temperature, and inlet Reynolds number

($\phi = 0.32$): larger φ resulted in high wall temperatures that endangered long-term catalyst stability. The lowest φ was dictated by homogeneous ignition requirements: for $\phi < 0.28$, homogeneous ignition was not guaranteed for the lowest flowrate of Table 1 even when the heaters were operated at full power. Homogeneous ignition requirements determined also the lowest flow rate ($U_{IN} = 1.6$ m/s); gas-phase combustion could not be sustained at $U_{IN} < 1.6$ m/s because of excessive heat losses. The highest flow rate was set by the requirement of maintaining a laminar flow in the channel. Finally, the adiabatic flame temperatures were, for $T_{IN} = 312$ K, 1149.4 K ($\varphi = 0.28$), and 1249.5 K ($\varphi = 0.32$).

Laser Diagnostics

The PLIF and Raman set-up is depicted in Fig. 3. In the former experiment, a frequency-doubled Nd:YAG pulsed laser (Quantel YG781C20, 20 Hz repetition rate) pumped a tunable dye laser (Quantel TDL50) with a frequency-doubled radiation at 285.09 nm and a pulse duration of 15 ns. The laser beam was transformed into a vertical laser sheet by a cylindrical lens telescope and a 1-mm slit mask. The laser sheet had a height of 4 cm and propagated in a counterflow direction along the *x-y* symmetry plane from the exhaust side. Because only the central 7 mm of the laser sheet entered the combustor, it maintained a nearly uniform intensity distribution over the entire measuring area. To ensure optical accessibility to the wall surfaces, the laser sheet had a very small divergence in the *y*-direction. The pulse energy was low enough (0.5 mJ) to avoid saturation of the $A(v = 1) \leftarrow X(v' = 0)$ transition. The fluorescence of both OH (1-1) and (0-0) transitions at 308 and 314 nm, respectively, was collected at 90° through one of the quartz windows with a cooled intensified CCD camera (LaVision FlameStar 2F, 576 × 384 pixels) gated to 100 ns; the camera was equipped with a 105 mm focal length f/4.5 lens (Nikon UV Nikkor) and a dielectric bandpass filter centered at 310 nm. A 180 × 7 mm^2 section of the combustor was imaged on a 576 × 24 pixel area of the CCD. One hundred images were averaged to increase the signal to noise ratio. The OH PLIF was calibrated with absorption measurements performed with the vertical laser sheet crossing laterally (in the *z* direction) the combustion zone through both quartz windows. This arrangement provided the only possible through-access needed for the calibration and was the same as in earlier CH_4/air CST studies [12]. Details on the calibration can be found elsewhere [29].

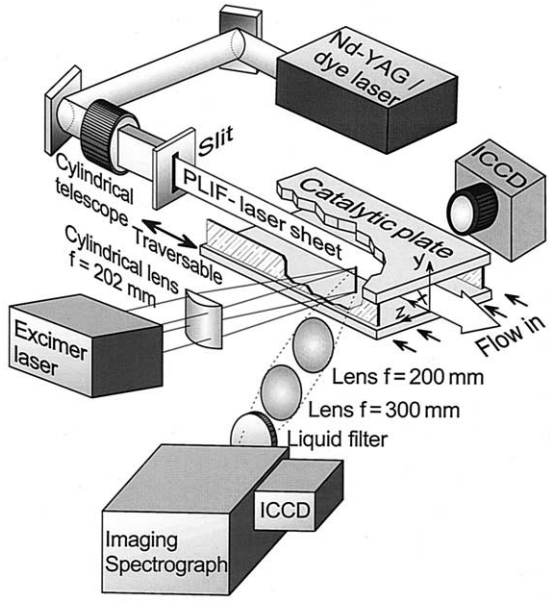

Fig. 3. Schematic of the OH PLIF and Raman experimental arrangement.

In the Raman measurements, a two-stage tunable narrowband KrF excimer laser (Lambda Physik Compex 150 T) was employed as excitation source. The first stage was used as a tunable oscillator and the second stage served as an amplifier in a single-pass arrangement. The pulse energy was 230 mJ at 248 nm, the repeti-

tion rate was 10 Hz and the pulse duration 20 ns. The rectangular, 25 mm × 9 mm, excimer beam profile was focused to a vertical line (~0.3-mm thick) inside the combustor by an f = 202 mm cylindrical quartz lens. The focal line spanned the entire 7-mm transverse extent of the channel and was about 15 mm offset from the x-y symmetry plane (z = 15 mm) to increase the collection angle and minimize beam steering effects. Because the combustion in the channel was strongly two-dimensional with no lateral dependence (except in regions extending up to ~15 mm from the quartz windows, as will be further discussed in the results section), the offset in the Raman measurements did not affect the forthcoming comparisons with the 2-D numerical predictions. The Raman signal was collected at 50° with respect to the sending optical path: two 70-mm diameter quartz lenses with f_1 = 200 mm and f_2 = 300 mm collected the Raman scattered light and focused it, with a magnification of 1.5, to the entrance slit of a 25-cm imaging spectrograph (Chromex 250i). The spectrograph was equipped with a second intensified CCD camera identical to that of the PLIF set-up; the 576 and 384 pixel dimensions of the recorded images corresponded to spectral range and channel height, respectively. A liquid filter with a path-length of 1 cm that contained 30% butyl acetate in UV-grade paraffin oil was placed before the spectrograph entrance to attenuate the intense Rayleigh signal. The excimer laser was tuned to a wavelength within the 248 nm KrF emission band that did not excite water vapor, OH radicals, or hot oxygen molecules [30]. The presence of windows and beam steering effects precluded the use of signal or laser beam retroreflectors. As the flow conditions were laminar, an average of 100 images was used to improve the signal-to-noise ratio. The spectral dispersion on the CCD camera ranged from 1250 cm^{-1} to 5000 cm^{-1} allowing observation of all major species (O_2, N_2, H_2O, and H_2); the Raman shift ranged from 1555 cm^{-1} (O_2) to 4155 cm^{-1} (H_2). The spectrograph slit was opened to 2 mm, resulting in a nearly top-hat slit transfer function with a width of about 200 cm^{-1}; an increased signal to noise ratio was thus attained without compromising the species spectral discrimination. The 7-mm channel height was resolved with 250 pixels. Raman measurements were acquired at streamwise intervals of 15 mm by traversing axially the combustor assembly. Both PLIF and Raman experiments had the advantage of near-wall access, in contrast to beam-crossing techniques (e.g., CARS).

The Raman data were referenced to a room temperature distribution of nitrogen inside the combustion channel. Determination of the effective Raman cross sections, which included transmission efficiencies of the detection system (e.g., windows, lenses, filter, spectrometer, and camera), was achieved by recording the signals of pure H_2, air, and completely burnt exhaust gases of known composition (the latter for assessing the cross section of H_2O). Despite the very efficient filtering of the Rayleigh signal, stray light could not be completely eliminated; the background signal was fitted to a polynomial curve to account for the spectral variation of the stray light contribution. An initial guess of the temperature distribution was derived from the nitrogen signal assuming ideal gas behavior. This distribution was then used to correct the temperature-dependent Raman cross sections. For the diatomic species, theoretical harmonic-oscillator Raman cross-section variations have been used [30]; for H_2O the data from Eisenberg [31] were employed. Using the corrected Raman cross-sections, an updated temperature was derived. Iterating a few times, resulted in a converged temperature distribution. Notwithstanding, the care in tuning the KrF wavelength, fluorescence contributions from oxygen hot-band transitions could not be ignored as they disturbed significantly the Raman oxygen signals. Therefore, the oxygen measurements were not considered in this study. The 250 pixel transverse extent was binned to 27 pixels, providing a y-resolution of 0.26 mm. Raman data points closer than 0.6 mm to both catalyst surfaces were discarded due to low signal-to-noise ratio.

NUMERICAL MODEL

Governing Equations and Boundary Conditions

The governing equations for a steady, laminar reactive flow with homogeneous and heteroge-

neous chemical reactions are, in their elliptic 2-D Cartesian form, as follows:

Continuity equation:

$$\frac{\partial(\rho u)}{\partial x} + \frac{\partial(\rho v)}{\partial y} = 0 \tag{1}$$

Momentum equations:

$$\frac{\partial(\rho uu)}{\partial x} + \frac{\partial(\rho vu)}{\partial y} + \frac{\partial p}{\partial x} - \frac{\partial}{\partial x}\left[2\mu \frac{\partial u}{\partial x} - \frac{2}{3} \cdot \mu\left(\frac{\partial u}{\partial x} + \frac{\partial v}{\partial y}\right)\right] - \frac{\partial}{\partial y}\left[\mu\left(\frac{\partial u}{\partial y} + \frac{\partial v}{\partial x}\right)\right] = 0 \tag{2}$$

$$\frac{\partial(\rho uv)}{\partial x} + \frac{\partial(\rho vv)}{\partial y} + \frac{\partial p}{\partial y} - \frac{\partial}{\partial x}\left[\mu\left(\frac{\partial v}{\partial x} + \frac{\partial u}{\partial y}\right)\right] - \frac{\partial}{\partial y}\left[2\mu \frac{\partial v}{\partial y} - \frac{2}{3}\mu\left(\frac{\partial u}{\partial x} + \frac{\partial v}{\partial y}\right)\right] = 0 \tag{3}$$

Energy equation:

$$\frac{\partial(\rho uh)}{\partial x} + \frac{\partial(\rho vh)}{\partial y} + \frac{\partial}{\partial x}\left(\rho \sum_{k=1}^{Kg} Y_k h_k V_{k,x} - \lambda \frac{\partial T}{\partial x}\right) + \frac{\partial}{\partial y}\left(\rho \sum_{k=1}^{Kg} Y_k h_k V_{k,y} - \lambda \frac{\partial T}{\partial y}\right) = 0 \tag{4}$$

Gas phase species equations:

$$\frac{\partial(\rho u Y_k)}{\partial x} + \frac{\partial(\rho v Y_k)}{\partial y} + \frac{\partial}{\partial x}(\rho Y_k V_{k,x}) + \frac{\partial}{\partial y} \cdot (\rho Y_k V_{k,y}) - \dot{w}_k W_k = 0, \quad k = 1,2, \ldots, K_g \tag{5}$$

Surface species coverage equations:

$$\frac{\partial \Theta_m}{\partial t} = \sigma_m \frac{\dot{s}_m}{\Gamma} - \frac{\Theta_m}{\Gamma}\dot{\Gamma}, \qquad m = 1, 2, \ldots, M_s. \tag{6}$$

The left side of Eq. 6 is not a true transient term and was introduced only to facilitate convergence to steady state. For heterogeneous reaction schemes that conserved the total number of sites, as the ones used in this study, the second term on the right side of Eq. 6 was identically zero. Gravity was not included in the y-momentum, as it was not important for the Reynolds numbers of this study.

The species diffusion velocities $\bar{V}_k$ were determined from the multicomponent diffusion equation [32]:

$$\nabla X_k = \sum_{l=1}^{K_g} \frac{X_k X_l}{D_{kl}}(\bar{V}_l - \bar{V}_k) + (Y_k - X_k)\frac{\nabla p}{p} + \sum_{l=1}^{K_g} \frac{X_k X_l}{\rho D_{kl}}\left(\frac{D_l^T}{Y_l} - \frac{D_k^T}{Y_k}\right)\frac{\nabla T}{T}, \quad k = 1, 2, \ldots K_g, \tag{7}$$

where D_{kl} are the multicomponent diffusion coefficients and D_k^T the species thermal diffusion coefficients. In addition to the full multicomponent approach, computations were also carried out with a simpler transport model, the mixture average diffusion plus thermal diffusion for the light species (Kee et al., [33])

$$\bar{V}_k = -[D_{km}/X_k]\nabla X_k + [D_{km}\theta_{T,k}/(X_k T)]\nabla T, \tag{8}$$

where D_{km} and $\theta_{T,k}$ are the mixture diffusion coefficient and the thermal diffusion ratio of the k-th species, respectively. Finally, the ideal gas and caloric equations of state were:

$$p = \rho RT/\bar{W} \text{ and } h_k = h_k^o(T_0) + \int_{T_0}^{T} c_{p,k}dT, \tag{9}$$

respectively. The set of Eqs. 1 through 6 supplemented with the auxiliary relations 7 and 9 was solved subject to the following boundary conditions. At the gas-wall interface ($y = 0$), the gas-phase species and energy boundary conditions were:

$$(\rho Y_k V_{k,y})_{y=0} = W_k \dot{s}_k \text{ and } T|_{y=0} = T_W(x), \tag{10}$$

respectively, with $T_w(x)$ the thermocouple-measured temperature distribution (average over the measured top and bottom plate profiles). No-slip boundary conditions were used at the wall for both velocity components. The inlet conditions were uniform profiles for the temperature T_{IN} (measured), the axial velocity U_{IN} (deduced from the measured mass flow rates and the inlet temperature) and the species compositions. Finally, zero-Neumann condi-

tions were used at the exit and the symmetry plane $y = b$.

Solution Algorithm

The governing set of equations was discretized using a finite volume approach. A SIMPLER [34] method was employed for the pressure-velocity field and solution was obtained iteratively using an ADI algorithm [35]. Computations were performed up to $x = 250$ mm, as the main event of interest (homogeneous ignition) occurred well within this extent and at the same time all of the fuel was practically consumed at $x = 250$ mm. An orthogonal staggered grid of 340×90 points (in x and y, respectively, with finer x-spacing and y-spacing towards the entry and the wall, repectively) was sufficient to produce a grid-independent solution. The coupling between the homogeneous and the heterogeneous phases was treated via time-splitting and a modified Newton method for the surface coverage (details are given in Refs. [11, 27]). The treatment of full multicomponent transport (Eq. 7) was new in the model and deserves more attention. An approach similar to channel-flow chemical vapor deposition studies [36] was adopted to avoid matrix inversion. Neglecting pressure-gradient diffusion, Eq. 7 can be recast to:

$$\rho Y_k \bar{V}_k = -\rho D_k \nabla Y_k - \rho D_k Y_k \nabla(\ln \bar{W}) + \bar{W} D_k Y_k \sum_{l=1,\, l\neq k}^{K_g} \frac{\rho Y_l \bar{V}_l}{W_l D_{kl}} - D_k^T \nabla(\ln T), \tag{11}$$

with D_k an effective species diffusion coefficient:

$$D_k = \left(\sum_{l=1, l\neq k}^{K_g} \frac{Y_l \bar{W}}{W_l D_{kl}} \right)^{-1}. \tag{12}$$

The first term on the right side of Eq. 11 was treated in the species transport equations (Eq. 5) as normal Fickian diffusion and the remaining terms as source. An explicit expression for the diffusion fluxes $\rho Y_k \bar{V}_k$ of species k could be derived from Eq. 11, provided that the diffusion fluxes of all other species were known: their values were evaluated at the previous iteration. For this purpose, each of the components of the species diffusion fluxes had to be stored at each node. This was the main disadvantage of the approach, as it required the storage of $2K_g$ additional variables (for a 2-D case) at every node. The computational time with the hetero/homogeneous reaction schemes described in the next section was ~24 h in an alpha cluster machine.

In addition to the elliptic model, a parabolic (boundary layer) model was also used (see, e.g., our previous work [15] or [37]), with elementary hetero/homogeneous chemical reaction schemes and detailed transport. The discretized set of equations (up to 450 grid points in the y-direction) constituted an algebraic-differential set of equations that was solved via marching in x. This approach resulted in substantially lower computational times (~15 min). The parabolic model was used only to assess its applicability—as a particularly efficient computational tool—in H_2/air CST. It will be shown that it had limited applicability under the conditions of this study.

Chemical Kinetics

Four homogeneous reaction mechanisms were investigated (see Table 2), further denoted as Warnatz [19], GRI-3.0 [20], Yetter [21], and Miller [22]. The CHEMKIN database was used for the gas-phase thermochemical [38] and transport properties [33]. An exception was the thermochemical data of HO_2: GRI-3.0 [20] and Yetter [21] suggested the HO_2 data from Hills and Howard [39] that resulted in a heat of formation of 3.0 kcal/mole compared to 2.5 kcal/mole [38]. However, when the HO_2 thermodata [38, 39] were interchanged in either the GRI-3.0 or Yetter schemes, there was no noticeable effect on the crucial part of this study, which is the onset of homogeneous ignition.

Three heterogeneous schemes for the H_2 oxidation on Pt were employed (see Table 3) further denoted as Deutschmann [5], Schmidt [6] and Kasemo [8]. The Schmidt and Kasemo schemes have been augmented with the addition of adsorption reactions for the H, O, and OH radicals (reactions 2, 4, and 6 in Table 3). Radical adsorption reactions play an important role in homogeneous ignition, as will be also discussed in the results section. It must be stated

TABLE 2

Homogeneous Chemical Reaction Mechanisms[a]

	Warnatz[b]			GRI 3.0[c]		
	A	b	E	A	b	E
H_2/O_2 reactions						
1. $H + O_2 = O + OH$	2.00×10^{14}	0.00	70.30	2.65×10^{16}	−0.67	71.30
$O + OH = H + O_2$		—			—	
2. $O + H_2 = H + OH$	5.06×10^{4}	2.67	26.30	3.87×10^{4}	2.70	26.19
3. $H_2 + OH = H_2O + H$	1.00×10^{8}	1.60	13.80	2.16×10^{8}	1.51	14.35
4. $OH + OH = O + H_2O$	1.50×10^{9}	1.14	0.42	3.57×10^{4}	2.40	−8.83
$O + H_2O = OH + OH$		—			—	
5. $H_2 + O_2 = OH + OH$		—			—	
H_2O_2 dissoc.-recombination						
6. $H + H + M = H_2 + M$	1.80×10^{18}	−1.00	0.00	1.00×10^{18}	−1.00	0.00
$H_2 + M = H + H + M$		—		—		
7. $H + H + H_2 = 2H_2$		—		9.00×10^{16}	−0.60	0.00
8. $H + H + H_2O = H_2 + H_2O$		—		6.00×10^{19}	−1.25	0.00
9. $O + O + M = O_2 + M$	2.90×10^{17}	−1.00	0.00	1.20×10^{17}	−1.00	0.00
10. $O + H + M = OH + M$		—		5.00×10^{17}	−1.00	0.00
11. $H + OH + M = H_2O + M$	2.20×10^{22}	−2.00	0.00	2.20×10^{22}	−2.00	0.00
HO_2 formation-consumption						
12. $H + O_2 + M = HO_2 + M$	2.30×10^{18}	−0.80	0.00	2.80×10^{18}	−0.86	0.00
$H + O_2 = HO_2$		—			—	
13. $H + 2O_2 = HO_2 + O_2$		—		2.08×10^{19}	−1.24	0.00
14. $H + O_2 + H_2O = HO_2 + H_2O$		—		1.13×10^{19}	−0.76	0.00
15. $H + O_2 + N_2 = HO_2 + N_2$		—		2.60×10^{19}	−1.24	0.00
16. $HO_2 + H = H_2 + O_2$	2.50×10^{13}	0.00	2.90	4.48×10^{13}	0.00	4.47
17. $HO_2 + H = OH + OH$	1.50×10^{14}	0.00	4.20	8.40×10^{13}	0.00	2.66
18. $HO_2 + H = H_2O + O$	3.00×10^{13}	0.00	7.20	3.97×10^{12}	0.00	2.81
19. $HO_2 + O = OH + O_2$	1.80×10^{13}	0.00	−1.70	2.00×10^{13}	0.00	0.00
20. $HO_2 + OH = H_2O + O_2$	6.00×10^{13}	0.00	0.00	1.45×10^{13}	0.00	−2.09
$HO_2 + OH = H_2O + O_2$		—		5.00×10^{15}	0.00	72.51
H_2O_2 formation-consumption						
21. $2HO_2 = H_2O_2 + O_2$	2.50×10^{11}	0.00	−5.20	1.30×10^{11}	0.00	−6.82
$2HO_2 = H_2O_2 + O_2$		—		4.20×10^{14}	0.00	50.21
23. $H_2O_2 + M = OH + OH + M$		—			—	
$H_2O_2 = OH + OH$		—			—	
24. $OH + OH + M = H_2O_2 + M$	3.25×10^{22}	−2.00	0.00	2.30×10^{18}	−0.90	−7.12
$OH + OH = H_2O_2$		—		7.40×10^{13}	−0.37	0.00
25. $H_2O_2 + H = H_2O + OH$	1.00×10^{13}	0.00	15.00	1.00×10^{13}	0.00	15.06
26. $H_2O_2 + H = H_2 + HO_2$	1.70×10^{12}	0.00	15.70	1.21×10^{7}	2.00	21.76
27. $H_2O_2 + O = OH + HO_2$	2.80×10^{13}	0.00	26.80	9.63×10^{6}	2.00	16.74
28. $H_2O_2 + OH = H_2O + HO_2$	5.40×10^{12}	0.00	4.20	2.00×10^{12}	0.00	1.79
$H_2O_2 + OH = H_2O + HO_2$		—		1.70×10^{18}	0.00	123.05

that the Schmidt and Kasemo schemes have been tested mainly on processes without gas-phase combustion, where the absence of radical adsorption was justified. The radical sticking coefficients of the added reactions were set to unity, as in Deutschmann's scheme. Implications of the addition of these reactions will be discussed in the results section. In Deut-

TABLE 2

(Continued)

Yetter[d]			Miller[e]		
A	b	E	A	b	E
1.91×10^{14}	0.00	68.78		—	
	—		4.00×10^{14}	−0.50	0.00
5.08×10^{4}	2.67	26.32	5.06×10^{4}	2.67	26.32
2.16×10^{8}	1.51	14.35	1.17×10^{9}	1.30	15.17
	—		6.00×10^{8}	1.30	0.00
2.97×10^{6}	2.02	56.07			
				—	
	—		1.70×10^{13}	0.00	199.91
	—		1.00×10^{18}	−1.00	0.00
4.58×10^{19}	−1.40	436.73		—	
	—		9.20×10^{16}	−0.60	0.00
	—		6.00×10^{19}	−1.25	0.00
6.16×10^{15}	−0.50	0.00	1.89×10^{13}	0.00	−7.48
4.71×10^{18}	−1.00	0.00	6.20×10^{16}	−0.60	0.00
2.21×10^{22}	−2.00	0.00	1.60×10^{22}	−2.00	0.00
3.50×10^{16}	−0.41	−4.69	3.61×10^{17}	−0.72	0.00
1.48×10^{12}	0.60	0.00		—	
	—			—	
	—			—	
	—			—	
1.66×10^{13}	0.00	3.43	1.25×10^{13}	0.00	0.00
7.08×10^{13}	0.00	1.26	1.40×10^{14}	0.00	4.49
	—			—	
3.25×10^{13}	0.00	0.00	1.40×10^{13}	0.00	4.49
2.89×10^{13}	0.00	−2.09	7.50×10^{12}	0.00	0.00
	—			—	
1.30×10^{11}	0.00	−6.82	2.00×10^{12}	0.00	0.00
4.20×10^{14}	0.00	50.12		—	
1.20×10^{17}	0.00	190.37	1.30×10^{17}	0.00	190.37
2.95×10^{14}	0.00	202.51		—	
	—			—	
	—			—	
2.41×10^{13}	0.00	16.61		—	
4.82×10^{13}	0.00	33.26	1.60×10^{12}	0.00	15.90
9.55×10^{6}	2.00	16.61		—	
1.00×10^{12}	0.00	0.00	1.00×10^{13}	0.00	7.53
5.80×10^{14}	0.00	39.99		—	

[a] Reaction rate coefficient $k = AT^{b}exp(-E/RT)$. Units: A [mole-cm-Kelvin-sec], E [kJoule/mole].

[b] Third body efficiencies: $\omega(H_2O) = 6.5$, $\omega(O_2) = \omega(N_2) = 0.4$ in reactions 6, 9, 11, 12, and 24.

[c] $\omega_6(H_2O) = \omega_6(H_2) = 0$, $\omega_9(H_2O) = 15.4$, $\omega_9(H_2) = 2.4$, $\omega_{10}(H_2O) = 6$, $\omega_{10}(H_2) = 2$, $\omega_{11}(H_2O) = 3.65$, $\omega_{11}(H_2) = 0.73$, $\omega_{12}(H_2O) = \omega_{12}(H_2) = \omega_{12}(N_2) = 0$, $\omega_{24}(H_2O) = 6$, $\omega_{24}(H_2) = 2$. Reactions 20, 21, and 28 are duplicate. Reaction 24 is a Troe reaction with parameters 0.7346, 94, 1756, and 5182 [38].

[d] $\omega(H_2O) = 12$ and $\omega(H_2) = 2.5$ in reactions 6, 9, 10, 11, 12, and 23. Reactions 21 and 28 are duplicate. Reactions 12 and 23 are Troe reactions with Fc = 0.5 [38] (first entries are the low pressure limits).

[e] $\omega_6(H_2O) = \omega_6(H_2) = 0$, $\omega_{10}(H_2O) = \omega_{11}(H_2O) = 5$, $\omega_{12}(H_2O) = 18.6$, $\omega_{12}(N_2) = 1.3$, $\omega_{12}(H_2) = 2.86$.

schmann's heterogeneous scheme, the reverse rates of reactions (7), (9), and (11) were calculated using the forward rate coefficients and surface thermochemical data [40]. The surface site density was $\Gamma = 2.7 \times 10^{-9}$ moles/cm^2 simulating polycrystalline platinum [5, 11]. The thick (2.2 μm) platinum layer on top of a non-porous Al_2O_3 layer closely resembled a

TABLE 3

Heterogeneous Chemical Reaction Mechanisms[a]

	Deutschmann[b]			Kasemo[c]			Schmidt[d]		
Adsorption Reactions	A (γ)	b	E	A(γ)	b	E	A (γ)	b	E
1. $H_2 + 2Pt(s) \rightarrow 2H(s)$	0.046	—	—	0.046	—	—	0.05	—	—
2. $H + Pt(s) \rightarrow H(s)$	1.0	—	—	1.0	—	—	1.0	—	—
3. $O_2 + 2Pt(s) \rightarrow 2O(s)$	0.07	—	—	0.023	—	—	0.003	—	—
4. $O + Pt(s) \rightarrow O(s)$	1.0	—	—	1.0	—	—	1.0	—	—
5. $H_2O + Pt(s) \rightarrow H_2O(s)$	0.75	—	—	0.7	—	—	0.1	—	—
6. $OH + Pt(s) \rightarrow OH(s)$	1.0	—	—	1.0	—	—	1.0	—	—
Surface Reactions									
7. $H(s) + O(s) \rightarrow OH(s) + Pt(s)$	3.7×10^{21}	0.0	11.5	3.7×10^{21}	0.0	11.5	3.7×10^{23}	0.0	10.5
8. $OH(s) + Pt(s) \rightarrow H(s) + O(s)$	from k_7 and $K_{c,7}$			3.7×10^{21}	0.0	24.5	3.7×10^{16}	0.0	21.0
9. $H(s) + OH(s) \rightarrow H_2O(s) + Pt(s)$	3.7×10^{21}	0.0	17.5	3.7×10^{21}	0.0	17.5	3.3×10^{25}	0.0	62.8
10. $H_2O(s) + Pt(s) \rightarrow H(s) + OH(s)$	from k_9 and $K_{c,9}$			3.7×10^{21}	0.0	113.5	6.7×10^{21}	0.0	155.0
11. $OH(s) + OH(s) \rightarrow H_2O(s) + O(s)$	3.7×10^{21}	0.0	48.2	3.7×10^{21}	0.0	48.2	3.7×10^{23}	0.0	51.5
12. $H_2O(s) + O(s) \rightarrow OH(s) + OH(s)$	from k_{11} and $K_{c,11}$			3.7×10^{21}	0.0	131.4		—	
Desorption Reactions									
13. $2H(s) \rightarrow H_2 + 2Pt(s)$	3.7×10^{21}	0.0	$67.4–6\Theta_H$	3.7×10^{21}	0.0	67.4	5.0×10^{12}	0.0	75.4
14. $2O(s) \rightarrow O_2 + 2Pt(s)$	3.7×10^{21}	0.0	$213.2–60\Theta_O$	3.7×10^{21}	0.0	213.2	5.0×10^{12}	0.0	218.0
15. $H_2O(s) \rightarrow H_2O + Pt(s)$	1.0×10^{13}	0.0	40.3	1.0×10^{13}	0.0	42.3	1.0×10^{13}	0.0	45.2
16. $OH(s) \rightarrow OH + Pt(s)$	1.0×10^{13}	0.0	192.8	1.0×10^{13}	0.0	192.8	1.5×10^{13}	0.0	201.1

[a] Reaction rate coefficient $k = AT^b exp(-E/RT)$. Units: A [mole-cm-Kelvin-sec] and E [kJoule/mole], except in the adsorption reactions whereby A denotes a sticking coefficient (γ). Surface species are denoted by (s).

[b] The hydrogen adsorption (reaction 1) is first order with respect to platinum. The oxygen sticking coefficient is temperature dependent: $\gamma_{O_2} = 0.07(T_0/T)$, with $T_0 = 300$ K. Reactions 8, 10, and 12 are the reverse of reactions 7, 9, and 11, respectively; their rates are calculated from the forward rates and surface thermochemical data [40].

[c] The hydrogen adsorption (reaction 1) is first order with respect to platinum.

[d] The hydrogen and oxygen adsorption (reactions 1 and 3) are first order with respect to platinum and the H(s) and O(s) desorption (reactions 13 and 14) first order with respect to the corresponding desorbing species. The O_2 adsorption is treated competitively as in Ref. [46]; the authors reported non-competitive O_2 adsorption in the case of methane [6].

polycrystalline platinum surface. The pre-exponential constants of all surface reactions in the Schmidt and Kasemo schemes (see Table 3) were recast to standard units (original units: sec^{-1}) using the chosen value of Γ. Gas phase and surface reaction rates were evaluated with CHEMKIN [41] and Surface-CHEMKIN [42], respectively. A set of hetero/homogeneous schemes will be further denoted by the assigned names of its constituent parts, the first entry always identifying the heterogeneous path: for example, Kasemo/Miller schemes. Finally, the prefix R or S will be used to denote a homogeneous or heterogeneous reaction, respectively, and the suffix (s) will denote a surface species.

RESULTS AND DISCUSSION

Experimental Results

The measured surface temperature distributions are depicted in Fig. 4. The profiles of Fig. 4 extend up to 250 mm (the range of interest for the present computations) and have been constructed by curve-fitting through the individual

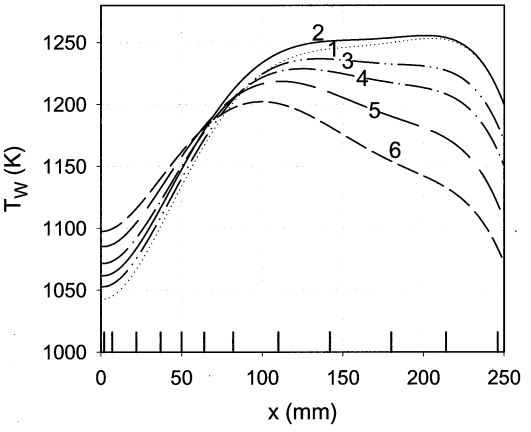

Fig. 4. Measured streamwise wall temperature profiles for the six cases of Table 1. The elongated tick-marks at the bottom of the figure indicate the thermocouple locations.

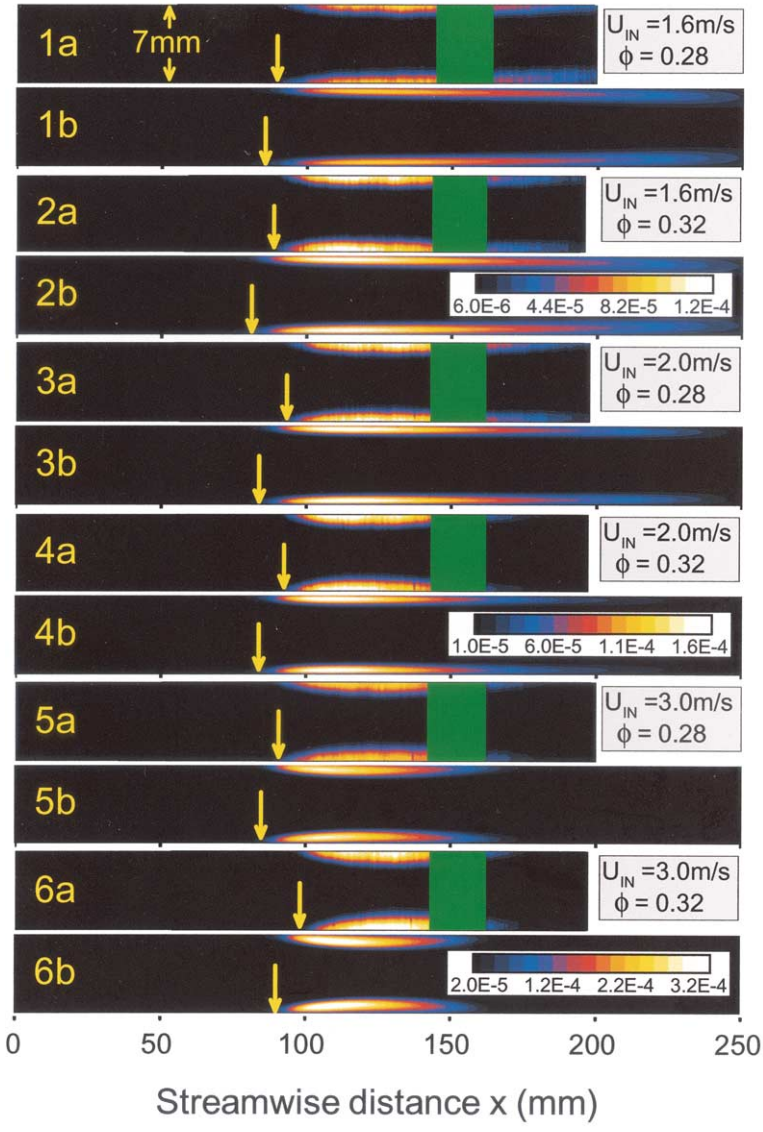

Fig. 5. Measured (1a-6a) and predicted (1b-6b) two-dimensional OH mole fraction distributions for the six cases of Table 1. The PLIF images extend up to $x = 194$ mm and are blocked around $x \approx 150$ mm (green bars) because of the window support-assemblies; each PLIF image is the average over 100 laser shots. The arrows indicate the onset of homogeneous ignition and the three color bars the OH levels for the pairs of Cases (1, 2), (3, 4), and (5, 6). The predictions (1b-6b) refer to the Deutschmann/Warnatz hetero/homogeneous schemes.

thermocouple measurements; the particular type of curve-fit did not influence the predicted homogeneous ignition characteristics. The suppression of the high entry temperatures (compare with Fig. 2) was evident: all profiles peaked at distances $x \geq 100$ mm. In addition, the surface temperatures were at the most 110 K (Case 1) higher than the corresponding adiabatic flame temperatures. Increasing U_{IN} (for $U_{IN} \geq 2$ m/s), led to lower temperatures at $x \geq 100$ mm. This was due to a reduction of the heaters' power: full power was applied in the lowest flow-rate Cases 1 and 2 and was progressively reduced with increasing case number from 95% (case 3) to 80% (case 6) of full scale.

PLIF-measured 2-D distributions of the OH mole fractions are illustrated in Fig. 5 along with numerical predictions obtained with the

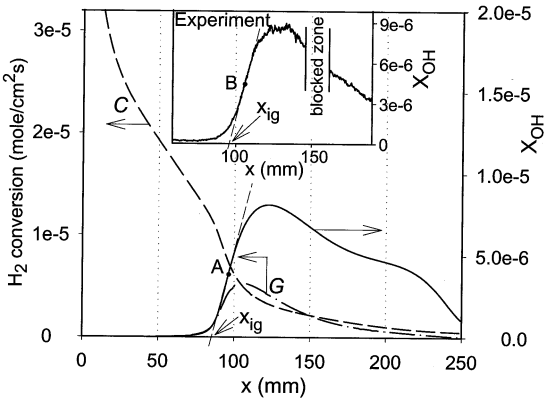

Fig. 6. Predicted (Deutschmann/Warnatz hetero/homogeneous schemes) streamwise profiles of the catalytic fuel conversion (C), the integrated (over the channel half-height b) gaseous fuel conversion (G) and the average (over b) OH mole fraction, for Case 3. The insert figure provides the corresponding average (over b) experimental OH profile. The onset of homogeneous ignition in both predictions and experiment is defined from the intersection with the x-axis of the tangent to the inflection points (A and B, respectively) of the OH profiles.

Deutschmann/Warnatz reaction schemes and the full elliptic model; these schemes were chosen as they provided the best agreement with the measurements. The blocked areas in the PLIF images corresponded to the location of the quartz window support-assemblies. The three color bars in Fig. 5 indicate the OH mole fractions (measured or predicted) for each of the three flow rates. The PLIF-measured OH levels of Fig. 5 were within 15% of the predicted ones, a reasonable agreement considering the PLIF experimental uncertainties and the small differences between the predicted and measured onset of homogeneous ignition. The homogeneous ignition locations (indicated by arrows in Fig. 5) have been determined with the aid of Fig. 6. Figure 6 provides, for Case 3, the measured and predicted streamwise profiles of the OH mole fractions (both averaged over $y = b$) as well as the numerically predicted profiles of the heterogeneous (C) and homogeneous (G) fuel conversions (the latter integrated over $y = b$). The sharp increase in the predicted OH or G profiles occurred essentially at the same distance. The OH profiles were used henceforth to define homogeneous ignition: the intersection of the tangent to the inflection point of the OH profile with the x-axis determined the homogeneous ignition distance (x_{ig}) in both experiments and predictions (see Fig. 6).

The Raman-measured transverse profiles of H_2, H_2O, and temperature at five selected streamwise distances are illustrated in Fig. 7 (Cases 1, 2, 3, and 5) along with the corresponding numerical predictions (to be discussed next) obtained using the Deutschmann/Warnatz schemes. The Raman data provided the only gas-phase information over the pre-ignition zone ($0 \leq x \leq x_{ig}$) because PLIF could not detect the very low levels of heterogeneously produced OH. The measurements of Fig. 7 extend as close as 0.6 mm from both walls, as stated in the experimental section. For reasons of clarity, ten out of the 27 transverse Raman points are shown in Fig. 7. The accuracy of the species Raman measurements was ~5% at volume concentrations greater than 4% and was reduced to ~20% at volume concentrations of 1%. It is worth pointing that mapping of major species and temperature distributions with nonintrusive measurements, such as those of Fig. 7, has not been reported yet in confined-flow catalytic combustion.

The stability and reproducibility of the flames with regard to their anchoring point (x_{ig}) and their symmetric shape was excellent over long measuring times. This was mainly a result of the prevalent two-dimensional flow characteristics: when traversing the OH laser sheet laterally in x-y planes as far as ±30 mm about the x-y symmetry plane, the flame characteristics remained unaltered. Only close to the quartz windows (±15 mm) the heat losses were sufficient to modify -albeit not strongly- the flame position. The side thermocouples ($z = \pm 40$ mm) indicated surface temperatures only 20 to 25 K lower than the symmetry plane thermocouples at the same x position. The sensitivity of the homogeneous ignition distance to small variations of the experimental conditions was assessed: experimental confidence intervals on x_{ig} were particularly useful, given its importance to the present investigation. Parametric numerical studies with the Deutschmann/Warnatz schemes were performed by varying U_{IN}, T_{IN}, φ, and the wall temperature distribution. Variation of the inlet velocity by ±5% produced no noticeable change in x_{ig}. Small variations in U_{IN} appear to be counteracted by finite rate surface

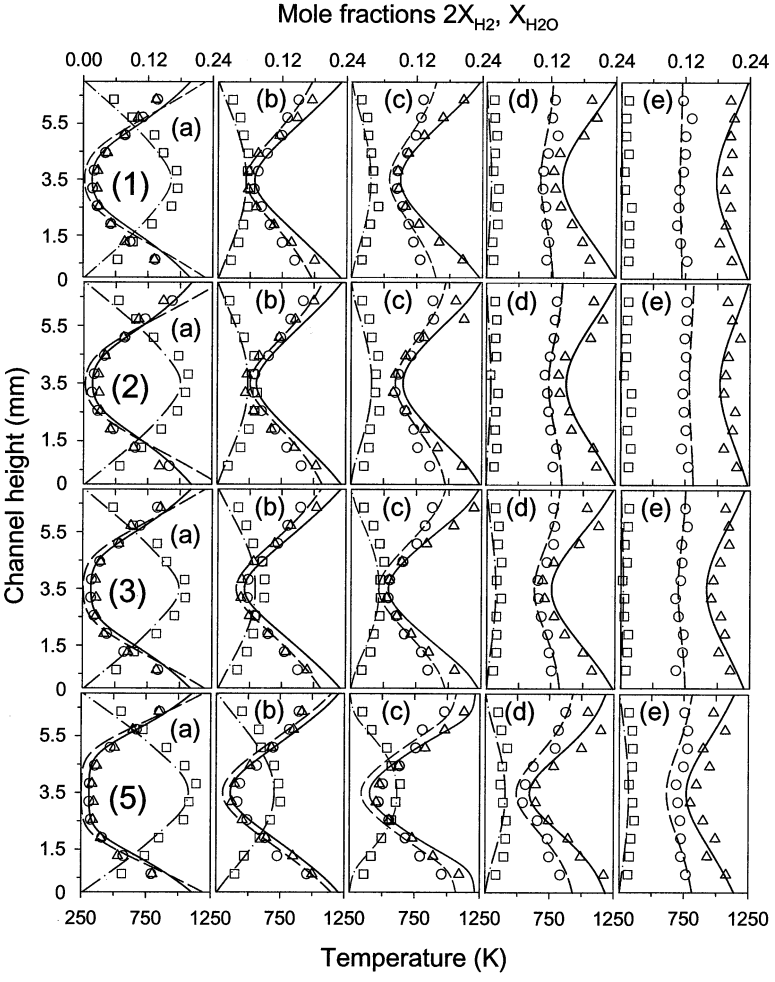

Fig. 7. Raman-measured and numerically predicted (Deutschmann/Warnatz schemes) transverse profiles of H_2, H_2O, and temperature at five selected streamwise locations: (a) $x = 25$, (b) $x = 85$ mm, (c) $x = 105$ mm, (d) $x = 165$ mm, and (e) $x = 235$ mm. The five rows from top to bottom represent Cases 1, 2, 3, and 5 of Table 1, respectively. For clarity, the H_2 mole fraction has been expanded by a factor of two. Symbols are measurements and lines numerical predictions. Squares: H_2, circles: H_2O, triangles: temperature. Dotted-dashed lines: H_2, dashed lines: H_2O, solid lines: temperature.

kinetic effects: a minor increase in U_{IN} resulted in increased transverse transport and hence in increased surface loading which, in turn, promoted homogeneous ignition due to the slight increase of the near-wall fuel levels. Variation of T_{IN} by ± 15 K altered x_{ig} by only ∓ 1.5 mm ($\sim 1.5\%$). Variation of φ by $\pm 2\%$ changed x_{ig} by about ∓ 1 mm ($\sim 1\%$). The above parameter variations were either equal to (in the case of φ) or twice as high as (in the case of U_{IN} and T_{IN}) their corresponding experimental uncertainties. To assess the sensitivity of x_{ig} on the wall temperature, an initial estimate was obtained for the deviation between the true catalyst surface temperatures and the thermocouple temperatures. An upper bound for this deviation could be obtained by setting the difference between the local surface heat generation ($\dot{q}_g$) and convection ($\dot{q}_c$) equal to the 1-D transverse heat conduction in the solid: $k_{eff}\,(T_{W,tr} - T_W) = \dot{q}_g - \dot{q}_c$, with T_W the measured temperature, $T_{W,tr}$ the true wall temperature and $1/k_{eff} = \sum_{i=1}^{3} d_i/\lambda_i$ the effective heat transfer coefficient that accounted for the type (Pt, Al_2O_3, and Si[SiC]) and depth (d_i) of the three materials through which heat was conducted. The computed $\dot{q}_g$ and $\dot{q}_c$ were used in this analysis. The resulting temperature difference

TABLE 4

Homogeneous Ignition Distances and Relative Heterogeneous Fuel Conversion[a]

Homogeneous Ignition Distance x_{ig} (mm)						Relative heterogeneous H_2 conversion at x_{ig}(%)
Case	Experiment	Warnatz	GRI-3.0	Yetter	Miller	
1	89.0	84.0	70.5	56.0	32.5	81.3
2	88.0	81.5	66.0	51.0	25.5	80.9
3	93.0	85.0	73.5	54.0	32.0	74.3
4	93.5	85.5	72.0	53.5	31.0	74.9
5	91.5	84.0	79.0	52.5	26.5	60.6
6	98.0	90.0	83.0	58.0	33.5	63.2

[a] The computed homogeneous ignition distances were obtained using four different gas-phase mechanisms and the heterogeneous mechanism of Deutschmann. The relative heterogeneous fuel conversion was computed with the Deutschmann/Warnatz hetero/homogeneous schemes.

$\Delta T = T_{W,tr} - T_W$ depended mainly on the x-location, then on the flow rate and, finally, mildly on φ. In the lowest flow-rate Cases 1 and 2, ΔT was as high as 5 K at x $\approx$ 0, dropping sharply to 0.5 K at x = 100 mm. The corresponding ΔT for the highest flow-rate Cases 5 and 6 were 8 K and 1.5 K, respectively. Using the corrected temperature profiles and computing anew, resulted in a decrease of x_{ig} by 0.8 mm for Cases 1 and 2 and by 2.0 mm for Cases 5 and 6. Overall, the combined experimental uncertainty in x_{ig} was estimated to ~1.5% (Cases 1 and 2), ~2.0% (Cases 3 and 4), and ~3.5% (Cases 5 and 6).

Effect of Gaseous Reaction Pathway on Homogeneous Ignition

Predicted (full elliptic computations with multicomponent transport) and measured homogeneous ignition characteristics are discussed next. Table 4 summarizes the measured and predicted x_{ig}, the latter obtained with the four homogeneous schemes and the heterogeneous scheme of Deutschmann. Concentrating firstly on the Deutschmann/Warnatz schemes, Fig. 5 had indicated a good agreement between measured and predicted x_{ig} (ranging from 5.6% to 8.6%). In addition, the extent and sweep angle of the flames of Fig. 5 were well predicted, as will be further elaborated in the flame-structure section. The predicted relative heterogeneous fuel conversion at the location of homogeneous ignition ranged from 81% to 60% (see Table 4). It is noted that the Raman measurements alone were not sufficient to determine the relative heterogeneous conversion (the streamwise velocity component was additionally needed). The relative heterogeneous conversions were then computed using the Deutschmann/Warnatz schemes; after all, these schemes reproduced well the experimental features of Figs. 5 and 7. The OH levels of Fig. 5 (measured or predicted) increased with increasing flow rate: this was a result of the increased amount of fuel available for gas-phase combustion with increasing U_{IN} (see Table 4). The fact that the measured x_{ig} of Table 4 differed by a maximum of 10 mm did not imply any similarity among the six experimental conditions. Cases 1 to 6 were quite different as they had significant variations in U_{IN} and fraction of fuel available for gaseous combustion, and adequate variations in $T_W(x)$ and φ. The rather narrow variation of x_{ig} was because of a counteraction between U_{IN} and $T_W(x)$: as stated before, increasing U_{IN} resulted in higher wall temperatures over the pre-ignition zone.

Different homogeneous schemes were examined in conjunction with the heterogeneous scheme of Deutschmann. Case 3 is used throughout the rest of this section as standard case; all other cases yielded qualitatively similar results. Figure 8 provides the computed local homogeneous fuel conversion profiles (integrated over $y = b$) for the four homogeneous schemes. As evidenced from Fig. 8, there is a substantial discrepancy among the predicted homogeneous ignition distances: the scheme of Warnatz underpredicted—on the average—the measured x_{ig} by 8%, GRI-3.0 by 20%, Yetter by 42%, and Miller by 66% (see Table 4). The local conversion rates of Fig. 8 were larger in the

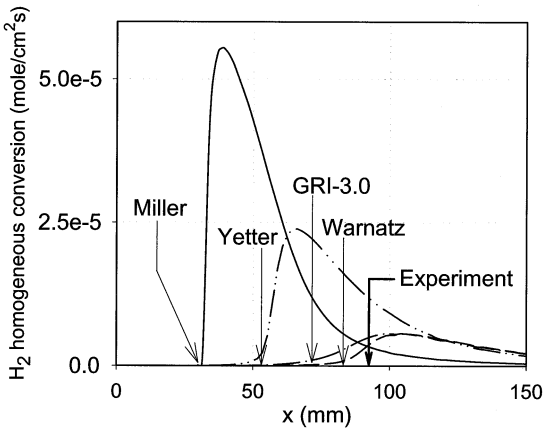

Fig. 8. Predicted streamwise profiles of homogeneous fuel conversions (integrated over the channel half-height b) using four different homogeneous schemes, (and the heterogeneous scheme of Deutschmann) for Case 3. The arrows indicate the onset of homogeneous ignition for each scheme; the experimental homogeneous ignition location is shown with the thick arrow. Homogeneous schemes: Miller (solid lines), Yetter (dashed-double dotted lines), GRI-3.0 (dotted-dashed lines) and Warnatz (dashed lines).

schemes with earlier ignition as they had larger amount of fuel available for gaseous combustion. Although the differences between measured and predicted x_{ig} are an essential part of this investigation, it is instructive for the present kinetic evaluation to define corresponding differences in ignition delay times. The local residence time $\tau(x)$ inside the channel was computed as:

$$\tau(x) = \int_0^x dx/\bar{U}(x), \tag{13}$$

with $\bar{U}(x)$ the local average (over $y = b$) streamwise velocity. The ignition delay times were evaluated as $\tau_d = \tau(x_{ig})$ and ranged from 20 to 34 ms in Warnatz's scheme to 8 to 12 ms in Miller's scheme. Such time scales and their differences were sufficiently long to be resolved in kinetic experiments (see, e.g., Ref. [21]). Hence, the x_{ig} differences of Fig. 8 reflected realistic kinetic effects and were not attributed to a convenient choice of experimental parameters (very high flow rates, e.g., very low residence times). Furthermore, such residence times were typical to CST power generation applications (4–25 ms [1,2]). The differences in predicted x_{ig} (or τ_{ig}) imparted an important aspect of the Raman data. Notwithstanding near-wall limitations, the Raman measurements provided an estimate of the catalytic reaction strength from the y-profile shape of the deficient reactant (H_2) for example, transport-limited, moderately or strongly kinetically controlled catalytic reactions. Such information was crucial since the same x_{ig}—although not necessarily the same ensuing flame structure—could be computed by many different sets of hetero/homogeneous schemes: given the fact that the heterogeneously-induced fuel depletion inhibited homogeneous ignition, a slow heterogeneous scheme would result in near-wall fuel excess which, in turn, when coupled to a slow homogeneous scheme could produce the same x_{ig} with that of a faster catalytic scheme (more pronounced near-wall fuel depletion) coupled to a faster homogeneous scheme. The predicted very low H_2 wall levels in the pre-ignition zone (see Fig. 7) indicated that the catalytic fuel conversion was, in the scheme of Deutschmann, practically mass-transport limited in all cases. The good agreement between the measured and predicted pre-ignition transverse hydrogen profiles supported the previous outcome and, moreover, suggested that the homogeneous pathway was responsible for the differences between measured and predicted x_{ig} of Fig. 8. This conclusion will be reinforced in the heterogeneous pathway discussion of the next section.

To understand the origin of the large differences of Fig. 8, sensitivity analysis (SA) was performed in all homogeneous schemes. The pre-exponential constant of each gas-phase reaction was multiplied (divided) by a given factor K, and the x_{ig} were computed anew. The (unaltered) heterogeneous scheme of Deutschmann was used in the SA. Factors K of 1.2, 1.5, and 2 were used and they all produced the same set of significant reactions. Figure 9 illustrates the percentage change in x_{ig} for the six most important reactions of every homogeneous scheme and for a multiplication (black bars) or division (grey bars) factor $K = 2$. All homogeneous schemes produced not only the same set of important reactions but also the same order of significance, except possibly small differences in the order of R3 and R17. The two most important reactions in all schemes were the chain

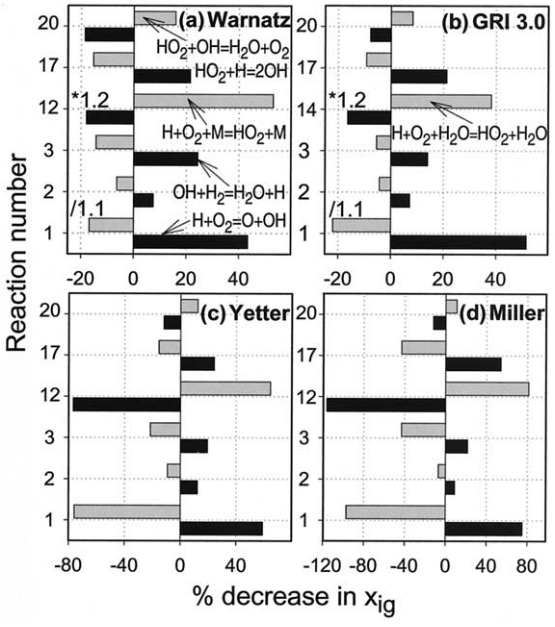

Fig. 9. Sensitivity analysis on four homogeneous schemes (and the heterogeneous scheme of Deutschmann), Case 3. The six most significant reactions of each gas-phase scheme are shown. The black bars indicate the percentage decrease in homogeneous ignition distance (x_{ig}) for a reaction rate multiplication by a factor of 2 and the gray bars for a division by the same factor. Exceptions are the reactions 1 in (a) and (b) (division by 1.1) and reactions 12 and 14 in (a) and (b), respectively (multiplication by 1.2).

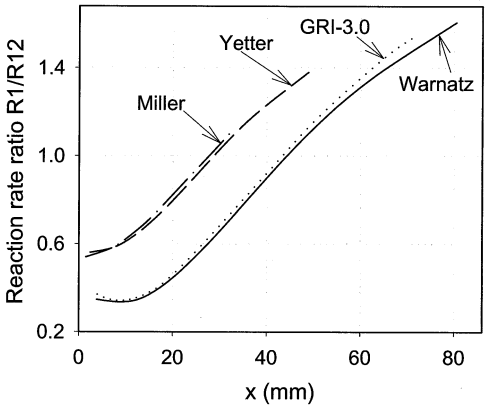

Fig. 10. Streamwise profiles of the ratio of the branching over terminating rates R1/R12 (see Table 2), Case 3; predictions with four homogeneous schemes and the heterogeneous scheme of Deutschmann. In GRI-3.0, the ratio R1/(R12+R13+R14+R15) was used instead of R1/R12. In Miller's scheme R1/R12 was negative since R1 was given for the reverse reaction (see Table 2); its absolute value was used for conformity with the other schemes. The ratios refer to the transverse locations of maximum hydrogen production rate $\frac{-1}{C_{H2}}\dot{w}_{H2}$. Solid lines: Warnatz, dotted lines: GRI-3.0, dashed lines: Yetter, dashed-dotted lines: Miller.

branching H + O_2 = O + OH (R1) and terminating H + O_2 + M = HO_2 + M (R12) steps, the latter leading to the relatively inactive HO_2 radical. In GRI-3.0, the terminating step was spread in reactions R12 through R15 (see Table 2) depending on the nature of the third body. R14 (M = H_2O) was the most sensitive, followed by R15 (M = N_2); the sensitivity of R15 was one-third of R14 and although its magnitude warranted inclusion in Fig. 9b, it was kept aside to retain the same reaction sets in Figs 9a-9d. Note that although the parameters for R1 in Miller's scheme were given for the reverse reaction (see Table 2), R1 proceeded in the branching direction (the R1 rate was negative). Finally, in the Warnatz and GRI-3.0 schemes, the multiplication factors of R12 and R14 were 1.2 and the division factors of R1 were 1.1. These schemes ignited farther downstream (see Fig. 8) and had, therefore, less amount of fuel available for gaseous combustion; an inhibition of homogeneous ignition through a decrease in R1 or increase in R12 (R14) by a factor of two, led to complete consumption of the fuel via the catalytic pathway and hence in no homogeneous ignition.

The streamwise profiles of the rate-ratio of the two most important reactions R1/R12, or R1/(R12 + R13 + R14 + R15) for GRI-3.0, are presented in Fig. 10 for Case 3. The rate-ratios were evaluated at transverse locations corresponding to the maximum hydrogen production rate, $\frac{-1}{C_{H2}}\dot{w}_{H2}$. The profiles of Fig. 10 extended ~5 mm upstream of the corresponding x_{ig} locations of each scheme. The Miller and Yetter schemes had (at any given x) the highest R1/R12, leading to a faster radical pool build-up. This is also evident from the computed transverse profiles (extending 1 mm away from the wall) of the H, O, and OH radicals presented in Fig. 11 at x = 28 mm, a pre-ignition location for all schemes. In the near-wall region, the Miller and Yetter schemes had 2.0 to 3.5 times higher radical levels than those of Warnatz's scheme. The profiles of Fig. 11 were dictated by the heterogeneous pathway. The wall-slopes of the O and H profiles were always positive (net-

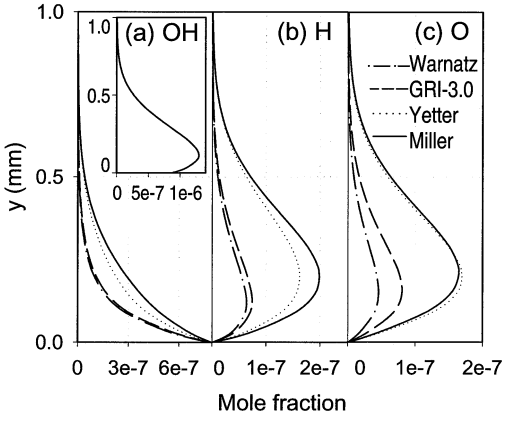

Fig. 11. Predicted transverse profiles of the OH, H, and O mole fractions for Case 3 at $x = 28$ mm. The transverse extent is 1 mm from the wall ($y = 0$). Four homogeneous schemes were used in the predictions (with the heterogeneous scheme of Deutschmann); Miller: solid lines, Yetter: dotted lines, GRI-3.0 dashed lines, Warnatz: dotted-dashed lines. The insert figure in (a) indicates the OH mole fraction at $x = 30$ mm for Miller's scheme.

adsorptive), indicating that the catalyst was a sink for both radicals; this was a result of the absence of O and H desorption steps (their desorption was recombinative). On the other hand, the OH flux was net-desorptive and the catalyst was, at least up to $x = 28$ mm, a source of OH radicals. However, this was not the case over the entire pre-ignition zone; in the insert of Fig. 11a, the OH profile of Miller's scheme at $x = 30$ mm had shifted to net-adsorptive. The corresponding shift to net-adsorptive OH flux occurred in the other schemes at 36.0 mm, 51.5 mm, and 72.5 mm (Yetter, GRI-3.0 and Warnatz, respectively). Hence, the catalytic wall was a sink of OH radicals in the latest pre-ignition stages. A similar behavior of the OH fluxes has been also reported in CH_4/air CST [11].

The differences in ignition predictions between the schemes of Yetter and Warnatz are firstly discussed. Because these schemes had essentially the same R1 reaction parameters (see Table 2), their significant ignition differences pointed to an examination of the termination step R12. Water was a very efficient third body in R12 and significant amounts of it were produced via the heterogeneous pathway (~21% per volume near the wall, see Fig. 7). The third body efficiencies of water in R12, $\omega_{12}(H_2O)$, were artificially changed in the Warnatz and Yetter schemes from their respective values of 6.5 and 12 to the corresponding efficiencies of N_2 (0.4 and 1.0, respectively), and x_{ig} were computed anew. The ignition distances (Case 3) were reduced from 85 to 31 mm (Warnatz) and from 54 to 29 mm (Yetter), the reduction being much more pronounced in Warnatz's scheme; the x_{ig} differences between the two schemes were thus drastically reduced both in absolute (2 mm) or relative (~6%) terms. Although GRI-3.0 was not elaborated in this study as it already had a reasonable agreement with Warnatz's scheme (within 15%, see Table 4), repeating the above procedure and setting the reaction parameters of R14 (M = H_2O) equal to that of R15 (M = N_2) improved mildly their agreement (12%). The key role of water in the predictions of Yetter's scheme was also confirmed with independent plug flow reactor (PFR) studies of gaseous mixtures under adiabatic, constant pressure conditions. The SENKIN package [43] was used to evaluate ignition delay times of gaseous mixtures with initial temperatures of 1,160 K (a temperature representative of the near-wall gas in the pre-ignition zone, see Fig. 7) and two different compositions: a $\varphi = 0.30$ H_2/O_2 mixture in an inert comprising of 21% vol. H_2O and 72% vol. N_2 (an inert composition representative of the near-wall gas over the pre-ignition zone) and then a $\varphi = 0.30$ H_2/O_2 mixture in 93% vol. N_2. The computed ignition delay times (defined as the inflection points of the temperature vs. time profiles) were in the first case 4.65×10^{-4}, 4.48×10^{-4}, and 3.42×10^{-4} sec and in the second case 2.99×10^{-4}, 2.96×10^{-4}, and 2.85×10^{-4} sec, for the Warnatz, GRI-3.0 and Yetter schemes, respectively. Again, a good agreement between the Yetter and Warnatz (or GRI-3.0) schemes was established. Therefore, the presence of water in the near-wall zone provided a plausible explanation for the origin of the large differences between the Warnatz and Yetter ignition predictions. A larger third body efficiency for H_2O in R12 appears, therefore, necessary in the scheme of Yetter.

A similar procedure was used to investigate the large underpredictions of x_{ig} obtained with Miller's scheme. Setting $\omega_{12}(H_2O) = \omega_{12}(N_2) = 1.3$ resulted in $x_{ig} = 16$ mm, that is the difference with Warnatz's scheme (31 mm) remained

very large. Similarly, the PFR studies yielded, for the $\varphi = 0.30$ H_2/O_2 mixture in 21% vol. H_2O and 72% vol. N_2, an ignition delay time of 2.72×10^{-4} sec (compare to 4.65×10^{-4} sec of Warnatz). For the H_2/O_2 mixture in 93% N_2, the ignition delay was 2.32×10^{-4} sec (compare to 2.99×10^{-4} sec of Warnatz). Hence, the presence of water was not the controlling factor for the significant underpredictions of Miller's scheme. It is worth pointing that a recent investigation [44] of NO_x formation in lean premixed methane/air combustion with comparative studies of various C/H/O/N schemes has shown a consistent overprediction of NO_x with Miller's scheme; this was attributed to the entire H/O reaction subset that predicted a faster radical pool build-up. The competition between R1 and R12 could be a possible source for the radical underprediction. Replacing R1 in Miller's scheme with that of Warnatz's scheme improved only mildly their agreement in x_{ig}. However, replacing Miller's R12 with that of Warnatz's (and keeping Miller's original third body efficiencies) yielded $x_{ig} = 83$ mm (Case 3), that is, essentially the same with that of Warnatz's scheme. The present study had thus shown that, under CST-relevant conditions, the radical pool was overpredicted in Miller's scheme, one possible reason being the underprediction of the terminating step R12.

Effect of Heterogeneous Reaction Pathway on Homogeneous Ignition

The sensitivity of homogeneous ignition on the reaction parameters of Deutschmann's scheme is firstly investigated. The pre-exponential constants of each heterogeneous reaction were multiplied (divided) by a given factor K and the x_{ig} were recomputed for all gas-phase schemes. Multiplication or division factors of $K = 10$ and $K = 20$ reproduced the same set of important reactions. The percentage change in x_{ig} for the eight most significant heterogeneous reactions and for $K = 20$ are illustrated in the SA of Fig. 12; for the most sensitive reaction (S1), the $K = 10$ results are presented. In adsorption reactions with a rate coefficient [11],

$$k_{ads,k} = \left(\frac{\gamma_k}{1 - \Theta_{Pt}\gamma_k/2} \right) \frac{1}{\Gamma^n} \sqrt{\frac{RT}{2\pi W_k}}, \qquad (14)$$

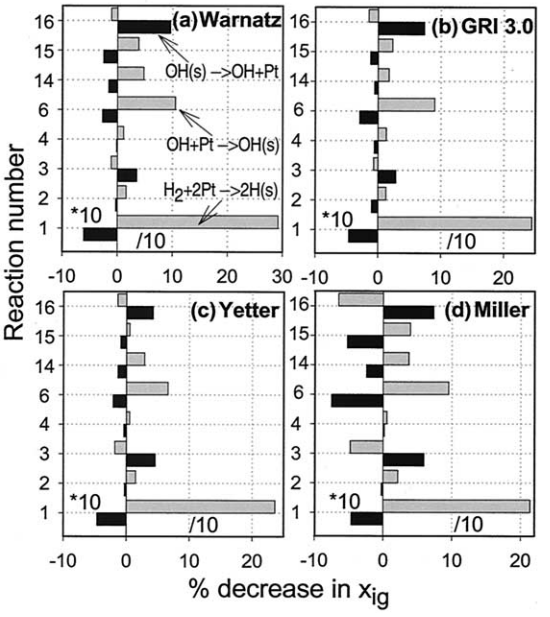

Fig. 12. Sensitivity analysis on the heterogeneous scheme of Deutschmann with four different homogeneous schemes, Case 3. The eight most significant heterogeneous reactions are shown. The black bars indicate the percentage change in homogeneous ignition distance (x_{ig}) for a heterogeneous rate multiplication by a factor of 20 and the gray bars for a division by the same factor; exception is reaction 1 with a factor of 10.

the factor K modified the bracketed term containing the species sticking coefficients. However, for the O, H, and OH radicals with the maximum allowable sticking coefficient of one, multiplication by K was meaningful on the collisional frequency (square-root term); this artificial increase was only intended to facilitate the SA discussion. The analysis of Fig. 12 should be seen with some caution; the wall temperature profile used in the SA was essentially established by the heterogeneous pathway itself. Key adsorption reactions (H_2 and O_2) determined the surface heat release and an excessive reduction of their rates or their ratio [7, 45] could inhibit light-off. On the other hand, radical adsorption/desorption reactions were not controlling the catalytic exothermicity. The SA of the former reaction set was thus strictly valid under the present prescribed wall temperature boundary conditions. It should be noted, however, that the uncertainty in the kinetic parameters of key heterogeneous reactions was

smaller than the variation explored in the SA of Fig. 12.

The SA of all gaseous schemes was qualitatively the same. Hydrogen adsorption (S1) was the most significant reaction as it determined the near-wall fuel depletion. The highly skewed bars in the SA of S1 reflected transport limitations. An increase of the rate coefficient of S1 by a factor of 10 increased x_{ig} by only 5 to 7% since the H_2 conversion was essentially transport-limited and the near-wall H_2-profile was not dictated by kinetics; a decrease of S1 by the same factor, however, decreased x_{ig} by up to 28% as the system shifted toward the kinetically controlled regime with a resulting near-wall fuel excess. Homogeneous ignition was particularly sensitive to the near-wall H_2 levels; a twofold decrease of S1, for example, resulted in still very low hydrogen wall levels but to an ~8% reduction in x_{ig} (Case 3). Excluding S1, all other reactions had a particularly small influence on x_{ig}. None of the purely surface reactions (S7-S12) were important in the SA of Fig. 12 as they were much faster than the adsorption or desorption reactions. Characteristically, a drastic decrease of the S7 through S12 reaction set by a factor $K = 10^4$ resulted in only a minor decrease of x_{ig} by 1 mm.

Next to S1 in significance were the OH adsorption and desorption (S6 and S16, respectively). The sensitivity of the O and H radical adsorption reactions (S4 and S2) was minimal. The O, H, and OH production rates at $x = 28$ mm are depicted in Figs. 13a to c and those of OH at $x = 78$ mm in Fig. 13d (Deutschmann/Warnatz schemes); the heterogeneous rates as well as the integrated rates (over $y =$ b) of the four most significant gaseous reactions are presented. The H and O adsorption rates were either smaller or comparable to the corresponding gas-phase production or destruction rates. In addition, the transverse profiles of Fig. 11 indicated transport-limited O and H adsorption fluxes (the wall levels of both O and H were $\sim 10^{-2}$ lower than the corresponding maximum levels inside the boundary layer). Although H was an important radical for gas-phase ignition (branching step R1), the heterogeneous path had a limited influence on it: an increase in S2 could not increase the transport-limited H adsorption flux and a corresponding decrease did not alter significantly the overall H production balance of Fig. 13a. A complete removal of H-adsorption reduced x_{ig} by only 3 mm (~3.5%). The O adsorption exhibited a similar behavior; a complete removal of O adsorption decreased x_{ig} by ~2%. On the other hand, the OH heterogeneous production or destruction rates were two orders of magnitude larger than the corresponding gas-phase rates at $x = 28$ mm (Fig. 13c) and an order of magnitude larger at $x = 78$ mm (Fig. 13d). In addition, the OH adsorption/desorption reactions were equilibrated throughout the pre-ignition zone: the net OH flux was ~100 times smaller than the corresponding adsorption or desorption fluxes. A reduction in S6 shifted the equilibrium to desorption, resulting in higher OH gaseous concentrations that, in turn, promoted the onset of homogeneous ignition. A complete removal of S6 altered drastically the OH production balance of Figs. 13c and d leading to a significant reduction of x_{ig} (by ~26% in Case 3). When all radical adsorption reactions (S2, S4, and S6)

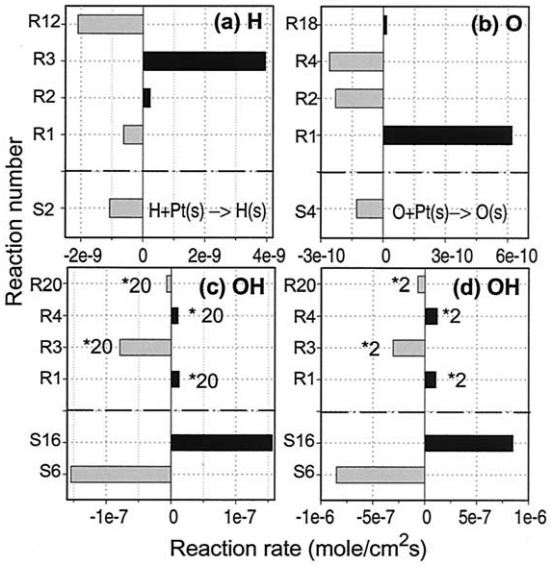

Fig. 13. Computed production (black bars) or destruction (gray bars) rates of the H, O, and OH radicals with the Deutschmann/Warnatz schemes, Case 3; the heterogeneous (S) and homogeneous (R) contributions are shown. In the homogeneous pathway, the four most significant homogeneous reactions are provided and their contribution is integrated over the channel half-height b; (a), (b), and (c) refer to $x = 28$ mm and (d) to $x = 78$ mm. For clarity, the OH homogeneous rates have been multiplied by 20 in (c) and by 2 in (d).

were removed, the reduction was (because of synergistic effects) ~40%; the synergies originated from the coupling of OH, H, and O via the branching or chain propagating reactions R1, R2, R3, and R4. The SA of Fig. 12a has thus indicated that the onset of homogeneous ignition could be correctly captured even with large uncertainties in the radical adsorption sticking coefficients ($0.05 \leq \gamma \leq 1$). Notwithstanding the significance of radical adsorption reactions, the degree of hetero/homogeneous radical coupling was determined by their net fluxes: when both OH adsorption/desorption reactions were removed, x_{ig} was reduced by only 10%. The heterogeneous pathway of OH, therefore, inhibited moderately homogeneous ignition. Although the OH flux was initially net-desorptive, it was the latest pre-ignition stages with net-adsorptive fluxes that determined the mild inhibition.

Numerical predictions with the schemes of Kasemo and Schmidt (in conjunction with the gaseous scheme of Warnatz) yielded (Case 3) a ≈5-mm earlier ignition ($x_{ig} \approx 80$ mm, compared to x_{ig} ~85 mm of Deutschmann's scheme). The combination of Kasemo or Schmidt schemes with any of the four gaseous schemes reproduced qualitatively the same x_{ig}-discrepancies with those reported in Table 4. Therefore, the following analyses will focus only on the gas-phase scheme of Warnatz. Despite the good agreement in the predicted x_{ig}, there existed significant differences in the underlying surface processes. The surface processes were investigated with the reaction flux diagrams of Fig. 14 ($x = 78$ mm) and the surface coverage of Fig. 15. The coverage of O(s) and H(s) is controlled by the wall concentrations of O_2 and H_2 and the adsorption rate ratio $k_{ads,O_2}/k_{ads,H_2}$ [7, 45]: under sufficiently fuel lean conditions, O(s) is the dominant coverage. The H_2 sticking coefficient was essentially the same in all schemes and, in addition, the H_2 adsorption was first order with respect to Pt (for the first order in Kasemo's scheme see Hellsing et al. [45]). The sticking coefficient of oxygen was, in Deutschmann's scheme, inversely proportional to the temperature (see footnote *b* of Table 3); as the wall temperature increased with increasing x over the entire pre-ignition zone, γ_{O_2} decreased and Θ_O dropped (see Fig. 15). In the scheme of Schmidt, a very fast initial rise of Θ_O was

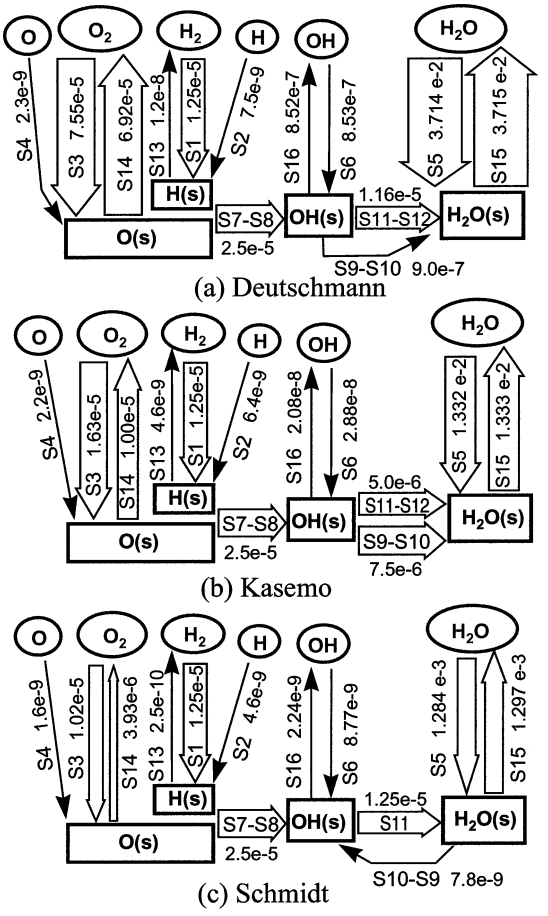

Fig. 14. Heterogeneous reaction flux analysis at $x = 78$ mm, Case 3: computations with three different heterogeneous schemes and the homogeneous scheme of Warnatz. Units: mole/cm^2 s. For clarity, the arrow-widths are not in scale.

evident at $x \approx 0$, followed by a slower increase down to $x \approx 80$ mm. The reason was the considerably lower O_2 adsorption rate of Schmidt's scheme at nearly uncovered conditions ($\Theta_{Pt} \approx 1$); comparison of the O_2 adsorption rates should be made between the effective terms $\gamma_{O_2}\Theta_{Pt}$ for Schmidt's first order adsorption [46, 6] and $\gamma_{O_2}\Theta_{Pt}^2$ for the other two schemes. The sharp drop of Θ_H and rise of Θ_O in Schmidt's scheme corresponded to a typical light-off [47] with a resulting light-off distance of ≈1.8 mm; in the other two schemes the light-off distances were practically zero.

In the scheme of Deutschmann, Θ_{OH}, Θ_H, and Θ_{H_2O} were controlled by thermodynamics: throughout the catalyst length, reactions S7/S8,

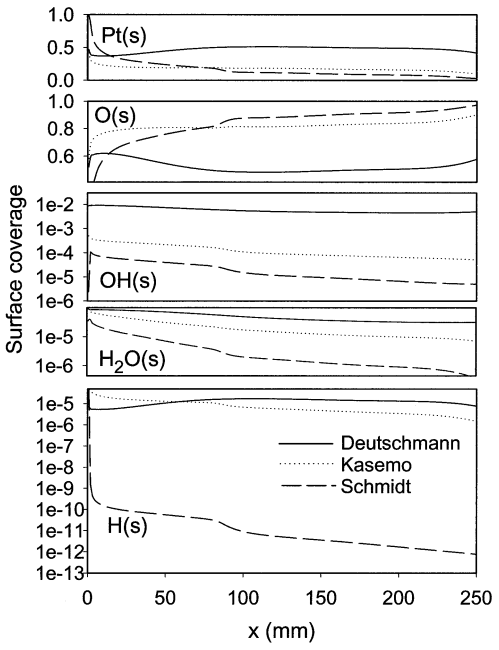

Fig. 15. Surface coverage, Case 3: predictions with three heterogeneous schemes and the homogeneous scheme of Warnatz. Solid lines: heterogeneous scheme of Deutschmann, dotted lines: Kasemo, dashed lines: Schmidt.

S9/S10, S11/S12, and S5/S15 were in partial equilibrium. The equilibrium conditions yielded,

$$K_{C,S7} \cong \frac{\Theta_{OH}\Theta_{Pt}}{\Theta_O\Theta_H}, \quad K_{C,S9}$$

$$\cong \frac{\Theta_{H_2O}\Theta_{Pt}}{\Theta_{OH}\Theta_H}, \quad K_{C,S11}$$

$$\cong \frac{\Theta_{H_2O}\Theta_O}{(\Theta_{OH})^2}, \quad K_{C,desH_2O}$$

$$\approx \frac{C_{H_2O,W}\Theta_{Pt}}{\Theta_{H_2O}}, \tag{15}$$

with $C_{H_2O,W}$ the wall concentration of water:

$$C_{H_2O,W} = X_{H_2O,W}p/RT_W. \tag{16}$$

Equations 15 and 16 related Θ_{OH}, Θ_{H_2O}, and Θ_H with Θ_O and Θ_{Pt} ($\approx 1 - \Theta_O$). The very low Θ_H levels (Fig. 15) indicated that the initiation step S7 of the surface pathway was limited by reactant coverage, a condition typical to mass-transport-limited operation.

In the scheme of Kasemo, the S7/S8 and the water adsorption/desorption reactions S5/S15 were equilibrated, but not the water formation steps S9/S10 and S11/S12. OH(s) was then depleted via S9 and S11, resulting in Θ_{OH} up to 30 times lower than those of Deutschmann's scheme. Under the transport-limited H_2 conversion, the hydrogen adsorption flux J_{ads,H_2} (the H_2 desorptive flux being minimal, see Fig. 14) was, at any given x-location ($x \geq 1.8$ mm in Schmidt's scheme), essentially the same (within 1%) in all schemes. Neglecting, to a first approximation, S9 in Deutschmann's scheme (it amounted to 8% of the water formation) and the reverse steps S10 and S12 in Kasemo's scheme (they amounted up to 20% of the corresponding forward rates S9 and S11), the following relations balance the H_2 flux and the water formation in both schemes:

$$J_{ads,H_2} \approx [k_{S11}\Gamma^2(\Theta_{OH})^2 - k_{S12}\Gamma^2\Theta_{H_2O}\Theta_O]_{DE}, \tag{17}$$

$$J_{ads,H_2} \cong [k_{S11}\Gamma^2(\Theta_{OH})^2 + k_{S9}\Gamma^2\Theta_{OH}\Theta_H]_{KA}, \tag{18}$$

with the subscripts *DE* and *KA* denoting the Deutschmann and Kasemo schemes. Using Eqs. 17 and 18 and noting that the rate coefficients k_{S11} were the same (Table 3), $(\Theta_{OH})^2_{DE} - (\Theta_{OH})^2_{KA} \approx [K^{-1}_{C,S11}\Theta_{H_2O}\Theta_O]_{DE} + [k_{S9}\Theta_{OH}\Theta_H]_{KA}/k_{S11}$, e.g., Θ_{OH} was lower in Kasemo's scheme. The implications of the lower Θ_{OH} were a considerably lower OH desorption flux for Kasemo's scheme ($J_{des,OH} = k_{des,OH}\Gamma\Theta_{OH}$). In the early pre-ignition zone where the gas-phase participation was weak, the OH adsorption/desorption reactions were close to equilibrium; therefore, a lower desorption flux implied lower near-wall OH levels for Kasemo's scheme. This is also illustrated in the transverse OH profiles of Fig. 16c, referring to $x = 28$ mm. Because of the reduced importance of the OH desorption path, the gas-phase pathway destroyed the OH adsorption/desorption equilibria in Kasemo's scheme. Moreover, the OH adsorption overtook the desorption rate in Kasemo's scheme at $x = 62$ mm (compare to $x = 72.5$ mm in Deutschmann's scheme), the net-adsorptive OH flux being higher than that of Deutschmann's scheme at the latest pre-ignition stages (Figs 14a-b). Thus, the OH heteroge-

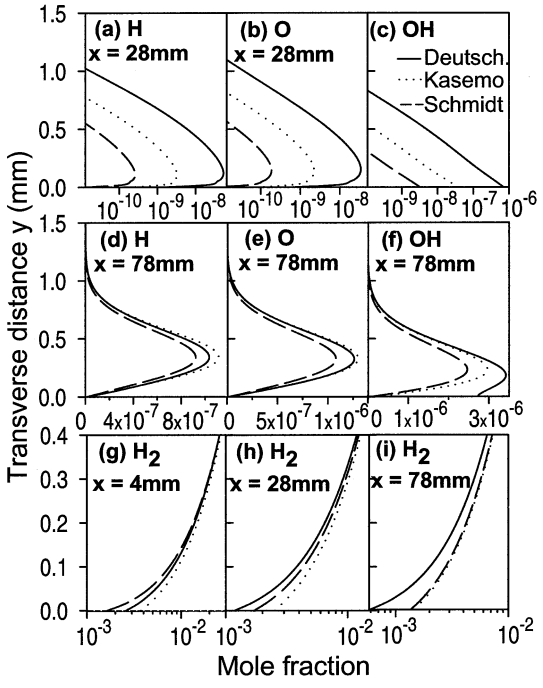

Fig. 16. Transverse profiles of radical and hydrogen mole fractions, Case 3. Predictions with three different heterogeneous schemes and the homogeneous scheme of Warnatz. (a)-(c): x = 28 mm, (d)-(f): x = 78 mm, (g): x = 4 mm, (h): x = 28 mm, and (i): x = 78 mm. Solid lines: heterogeneous scheme of Deutschmann, dotted lines: Kasemo, dashed lines: Schmidt.

neous route in Kasemo's scheme was—compared to Deutschmann's scheme—a stronger inhibitor of homogeneous ignition over the entire pre-ignition zone. Despite the stronger OH inhibition, however, the OH levels at the latest pre-ignition locations were in Kasemo's scheme only 15% lower than those of Deutschmann (see Fig. 16f) except very close to the wall where the OH levels of the latter scheme were still dictated by their adsorption/desorption equilibria. The H and O radicals (Figs. 16a, b, d, and e) at the latest pre-ignition stages were somewhat higher in Kasemo's scheme compared to Deutschmann's scheme. Although it can be considered that the gas-phase mechanism remained relatively unaffected by such changes in the OH, O, and H heterogeneous routes, there was an additional mechanism that promoted the radical build-up in Kasemo's scheme. The H_2 transverse profiles of Figs. 16g through i indicated a larger near-wall fuel excess for Kasemo's scheme compared to Deutschmann's scheme for reasons explained below. Even though this excess was not sufficient to disturb the magnitude of the hydrogen fluxes, it nevertheless promoted ignition. The good agreement between Kasemo's and Deutschmann's ignition predictions could be thus attributed to the counteracting effects of fuel-excess promotion and radical inhibition. The H_2 flux was, $J_{ads,H_2} = k_{ads,H_2} C_{H_2,W} \Gamma \Theta_{Pt}$, which yields:

$$C_{H_2,W} = J_{ads,H_2}/(k_{ads,H_2}\Gamma\Theta_{Pt}). \quad (19)$$

Because the rate coefficient $k_{ads,H2}$ was the same in both schemes and at the same time the H_2 fluxes were the same at any given x, $C_{H_2,W}$ was determined by Θ_{Pt}. Over the pre-ignition zone, $C_{H_2,W}$ was higher in Kasemo's scheme (Figs. 16g-i) compared to Deutschmann's scheme as the Θ_{Pt} in the former scheme was lower. With regard to the significance of radical adsorption reactions, their influence was less pronounced in Kasemo's scheme due to the reduced radical adsorption fluxes. Removing the OH adsorption reduced x_{ig} by 8% (compare to 26% in Deutschmann's scheme) whereas removal of all radical adsorption reactions led to a 24% reduction in x_{ig} (40% in Deutschmann's scheme). Although the significance of radical adsorption reactions was reduced in Kasemo's scheme, their addition was still necessary for accurate homogeneous ignition predictions.

In the scheme of Schmidt, reactions S7/S8 were far from equilibrium, S8 being of no significance; the result was a fast depletion of H(s) via S7. The surface coverage of H(s) and OH(s) could be then directly linked to the hydrogen flux considering the sequential path H_2 adsorption, S7, and finally S11. The H_2 adsorption and S7 yielded

$$2J_{ads,H_2} = [k_{S7}\Gamma^2\Theta_H\Theta_O]_{SC}, \quad (20)$$

the subscript SC indicating the scheme of Schmidt. Similarly, the balance between H_2 adsorption and S11 (the water formation route S9-S10 was minimal, see Fig. 14) yielded,

$$J_{ads,H_2} = [k_{S11}\Gamma^2(\Theta_{OH})^2]_{SC}. \quad (21)$$

Θ_{OH} in Schmidt's scheme was lower than that of Kasemo's scheme since k_{S11} in the former

scheme was about two orders of magnitude larger (see Table 3). Equation 21 yielded:

$$\Theta_{OH} = \sqrt{J_{ads,H2}/(k_{S11}\Gamma^2)}. \quad (22)$$

Θ_{OH} decreased sharply with increasing x because of the drop of the hydrogen flux. It is worth pointing that the resulting OH desorption flux $J_{des,OH} = k_{des,OH}\Gamma\Theta_{OH}$ was hydrogen-flux-limited in the scheme of Schmidt. The very low Θ_{OH} resulted to the lowest OH desorption rates (Figs. 14a-c) and OH levels (Fig. 16c) among all schemes. Thus, the heterogeneous OH inhibition was the strongest in the scheme of Schmidt; it was, nevertheless, counteracted by a near-wall H_2 fuel excess (Fig. 16i), similar to that of Kasemo's scheme. The importance of the added radical adsorption reactions was finally assessed; removal of OH adsorption reduced x_{ig} by only 6% because of the very low OH adsorption fluxes. When all radical adsorption reactions were removed, x_{ig} was reduced by 20%. Again, the presence of all radical adsorption reactions was shown to be necessary for accurate predictions of homogeneous ignition.

In conclusion, although there existed significant differences among the heterogeneous schemes in their surface coverage and radical fluxes, these differences had practically no impact on homogeneous ignition. The reason was that all schemes captured the measured mass-transport-limited H_2 conversion and, in addition, homogeneous ignition was rather insensitive to the magnitude of the radical fluxes. Finally, regarding the transport model, removal of thermal diffusion (last term in Eq. 7) reduced x_{ig} by up to 3 mm. When the simpler mixture-average diffusion transport with thermal diffusion was used (Eq. 8), the predictions were essentially the same with those of the full multicomponent model of Eq. 7.

Flame Structure and Applicability of the Parabolic Model

The structure of the established flames is firstly addressed. Figures 17a and b provide computed 2-D maps of the H_2 mole fraction (a logarithmic color scale was used to emphasize the post-ignition low hydrogen levels), the iso-contours of the H_2 reaction rate, and the flow field velocity vectors for Cases 3 and 5 (Deutschmann/Warnatz schemes). Predictions from the Deutschmann/Miller schemes are given in Fig. 17c (Case 3). Although the scheme of Miller did not reproduce the experiments, it was included to facilitate the ensuing discussion on the applicability of the parabolic model. The dashed lines in Figs 17a and b delineate the flame envelope as determined by the computed visible blue OH levels of Figs. 5 3b and 5b). The blue flame tails were overpredicted in the weaker flames (Cases 1–4); however, this can be attributed to the corresponding very low OH levels (20–50 ppm) at the flame tails that are difficult to detect with a planar technique. Furthermore, predictions and Raman measurements of the H_2 were in good agreement as indicated in Figs. 7 (3 and 5); the Raman profiles clearly illustrated the stronger streamwise fuel depletion for the lower flow rate Case 3 compared to that of Case 5. The reaction iso-contours indicated a well-defined flame structure established (Case 3) in the region 85 mm $< x <$ 130 mm. Most of the gaseous conversion occurred in this range (see also the G curve of Fig. 6). Farther downstream, in most of the flame envelope of Fig. 17a, the H_2 levels were low enough that, in conjunction with the local temperature, could not support a flame; gaseous conversion occurred in a distributed manner as indicated by the widely-separate iso-contour levels. The flame envelope of Case 5 (Fig. 17b) was narrower than that of Case 3 (Fig. 17a) as the wall temperature was lower in the former case at $x > 150$ mm. Throughout the entire post-ignition zone, the heterogeneous mode converted fuel in parallel to the homogeneous mode (see also the C and G curves of Fig. 6); fuel leaked through the gaseous combustion zone, to be converted subsequently on the catalytic wall. Fuel leakage was more pronounced in the higher velocity Case 5 (see the more noticeable wall gradient $[(dX_{H2}/dy)_{y=0}$ of Fig. 7 (5d) compared to that of (3d)]. Fuel leakage through the gaseous zone in hetero/homogeneous combustion was firstly reported in stagnation point flow studies [48] of fuels with Le <1, under increased strain rate conditions. In our recent turbulent H_2/air CST numerical studies [27], fuel leakage was more pronounced with decreasing φ or increasing turbulent transport.

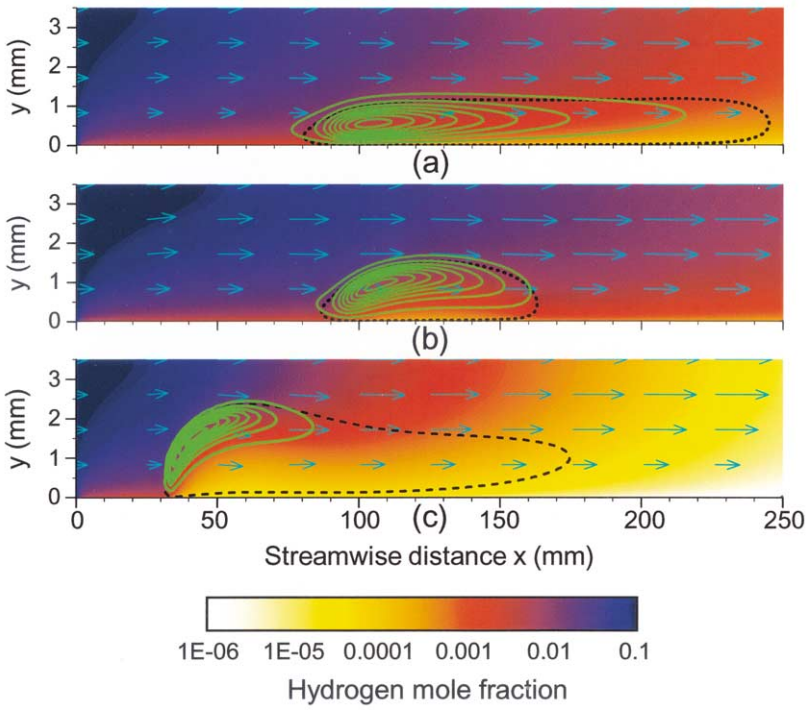

Fig. 17. Two-dimensional color maps of the computed H_2 mole fractions, the velocity vectors and the H_2 reaction rate ($-w_{H_2}$) iso-contours: (a) Case 3, Deutschmann/Warnatz schemes, (b) Case 5, Deutschmann/Warnatz schemes, (c) Case 3, Deutschmann/Miller schemes. The black dotted lines in (a) and (b) delineate the flame envelope as defined by the visible bluish OH levels in Fig. 5 (3b and 5b, respectively). In (c) the flame envelope was defined in an analogous manner. The velocity vectors scale according to their entry ($x = 0$) magnitudes: 2 m/s in (a) and (c) and 3 m/s in (b). The H_2 iso-contour reaction rate levels, $-w_{H_2}$, are: (a) inner contour 7.8×10^{-5} mole/cm^3 s and increment 4.9×10^{-6} mole/cm^3 s, and (c) inner (b) inner contour 4.0×10^{-4} mole/cm^3 s and increment 2.5×10^{-5} mole/cm^3 s, and (c) inner contour 2.7×10^{-3} mole/cm^3 s and increment 1.7×10^{-4} mole/cm^3 s.

Catalytic combustion was the dominant fuel conversion mode farther downstream; it became the sole fuel conversion mode at sufficiently large x, where H_2 levels were too low to support any gaseous combustion (see the C and G conversions of Fig. 6 at 240 mm $\leq x \leq$ 250 mm).

The flames of Figs. 17a and b were confined close to the wall. This was a result of the low Lewis number of hydrogen; fuel was transported more efficiently toward the wall than heat away from it, confining the combustion wave close to the wall (see also [27, 48]). For example, the computations (or Raman data) of Fig. 7 (3c) indicated that, at $x = 105$ mm, the hydrogen depletion was already sensed at the channel center ($X_{H_2,y=3.5}/X_{H_2,IN} = 0.28$) whereas the corresponding mixture heating was not (using an average wall temperature $\bar{T}_W =$ 1,140 K over the zone $0 \leq x \leq 105$ mm, $(\bar{T}_W - T_{y\,=\,3.5})/(\bar{T}_W - T_{IN}) = 0.76$). When the diffusivity of H_2 was artificially reduced by a factor of three (so that $Le \approx 1$), the computed gaseous flame propagated directly to the channel center.

Finally, the applicability of the parabolic model is addressed. The average flame sweep angle (acute angle of the flame with respect to the x-axis) of Case 5 (Fig. 17b) was larger than that of Case 3 (Fig. 17a) as the former case had a larger amount of fuel available for gaseous combustion (see Table 4). The flame of Fig. 17b was stronger than that of Fig. 17a, having a higher local laminar flame speed; the sweep angle of the flame was, in turn, determined by the magnitude of the local laminar flame speed and the local flow velocity (see also [15]). In the flame of Fig. 17c, with an even higher amount of fuel available for gaseous combustion, the flame sweep angle was the highest. In recent studies [15] we delineated the regimes of applicability

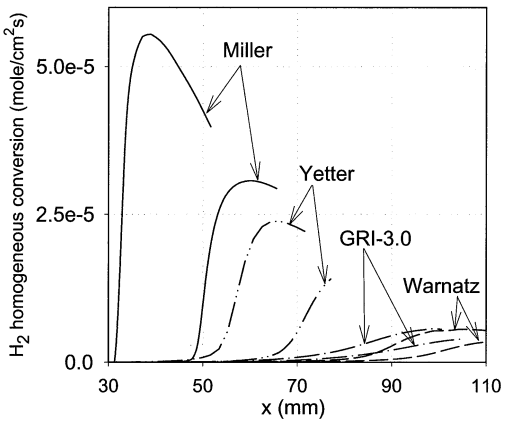

Fig. 18. Computed homogeneous fuel conversions with four homogeneous schemes and the heterogeneous scheme of Deutschmann, Case 3. For every homogeneous scheme two model predictions are shown, an elliptic and a parabolic one. The elliptic predictions are always those with earlier ignition (earlier rise of the fuel conversion curves). Dashed lines: Warnatz homogeneous scheme, dashed-dotted lines: GRI-3.0, dashed-double dotted lines: Yetter, solid lines: Miller. For clarity, only the initial rise of the homogeneous conversion is shown in the last three schemes.

of the parabolic model in assessing homogeneous ignition of CH_4/air CST. It was shown that, for a given inlet equivalence ratio, there existed a minimum inlet velocity $U_{IN,min}$ above which both the elliptic and parabolic models yielded the same ignition distances. For $U_{IN} < U_{IN,min}$, the flame sweep angle was large enough so that the streamwise component of the flame was significant; since the parabolic model lacked streamwise diffusion, its absence of upstream flame propagation resulted in a later ignition compared to that of the elliptic model. Homogeneous ignition predictions (with all four gaseous schemes and the heterogeneous scheme of Deutschmann) are illustrated in Fig. 18 with both elliptic and parabolic models. Although the parabolic model captured the correct ignition sequence, the corresponding ignition distances were -as expected- larger than those of the elliptic model; moreover, their relative discrepancy increased from ~15% in the Deutschmann/Warnatz schemes to ~50% in the Deutschmann/Miller schemes due to the corresponding increase in the flame sweep angle (see Figs. 17a and 17c). These discrepancies were only marginally improved in the highest flow rate Cases 5 and 6. Because the highest flow rates of the present work were close to the laminar flow limit (laminar flow had to be maintained for kinetic evaluation studies), it was concluded that in laboratory-scale burners the applicability of the parabolic approach was limited. The parabolic model could provide useful trends with very high computational efficiency, but not quantitative results.

CONCLUSIONS

The catalytically stabilized combustion of lean H_2/air mixtures was investigated numerically and experimentally at atmospheric pressure in laminar channel-flow configurations. Measured homogeneous ignition distances (x_{ig}) were compared against numerical predictions using a 2-D elliptic fluid mechanical model with multicomponent transport and elementary hetero/homogeneous reaction schemes; four different homogeneous and three heterogeneous schemes were tested. The following are the key conclusions of this study.

1. The numerically predicted homogeneous ignition distances (x_{ig}) underpredicted the measurements by 8% to 66% depending on the particular hetero/homogeneous reaction schemes. These differences were ascribed primarily to the homogeneous reaction pathway, the heterogeneous pathway having only a small influence on x_{ig}.
2. The gas-phase scheme of Warnatz gave the best agreement to the measured x_{ig} (~8% underprediction), followed by GRI-3.0 (~20% underprediction), Yetter (~42% underprediction), and Miller (~66% underprediction). Sensitivity analysis identified the key reactions affecting homogeneous ignition; the most sensitive reactions in all schemes were the chain branching and terminating steps $H + O_2 = OH + O$ and $H + O_2 + M = HO_2 + M$, respectively. The large underpredictions of Yetter's scheme were ascribed to the presence of large amounts of water (produced via the heterogeneous reaction pathway) due its effectiveness as a third body in the terminating step. The even larger underpredictions of Miller's scheme were attributed to its faster radical pool build-up.
3. The heterogeneous reaction pathway had a

particularly small influence on homogeneous ignition. Computations with the homogeneous scheme of Warnatz indicated that the heterogeneous scheme of Deutschmann underpredicted x_{ig} by ~8% and the schemes of Kasemo and Schmidt by ~13%. Notwithstanding the small differences in x_{ig}, there existed significant variations among the heterogeneous schemes in their surface coverage and magnitude of radical fluxes. Sensitivity and reaction path analyses showed that the good agreement in x_{ig} was attributed to the fact that all heterogeneous schemes captured the measured transport-limited catalytic fuel conversion and to the relative insensitivity of homogeneous ignition on the magnitude of the radical fluxes, provided that all radical adsorption reactions were included in the heterogeneous schemes. Finally, a mild homogeneous ignition promotion via near-wall fuel excess appeared to be counteracted by a somewhat stronger radical flux inhibition in the Schmidt and Kasemo schemes.

4. The presence of OH, H, and O radical adsorption reactions (primarily OH adsorption), was essential in all heterogeneous schemes for accurate homogeneous ignition predictions. The OH adsorption inhibition was stronger in the scheme of Deutschmann, followed by the schemes of Kasemo and Schmidt. This was because of a corresponding reduction (in the same scheme-order as before) of the magnitude of the radical adsorption fluxes.
5. Following homogeneous ignition, very stable flames were established, confined close to the catalytic wall due to the diffusional imbalance of hydrogen. The numerical predictions and the Raman measurements indicated that fuel leaked through the gaseous combustion zone, resulting in a combined homogeneous-heterogeneous fuel conversion.
6. A parabolic model was tested and shown to have limited applicability in reproducing the measured homogeneous ignition characteristics. Although the parabolic and elliptic models were in reasonable agreement when predicting weak flames, in stronger flames the former model predicted homogeneous ignition distances up to 50% larger than those of the latter.

Support for this work was provided by the Swiss Federal Office of Energy (BFE) under contract No. 59048 and Alstom Power Technology of Switzerland.

REFERENCES

1. Dalla Betta, R. A., and Rostrup-Nielsen, T., *Catalysis Today* 47:369–375 (1999).
2. Beebe, K. W., Cairns, K. D., Pareek, V. K., Nickolas, S. G., Schlatter, J. C., and Tsuchiya, T., *Catalysis Today* 59:95–115 (2000).
3. Catalytica Inc., press release, Dec. 14, 1999, http://www.catalytica-inc.com.
4. Deutschmann, O., Behrendt, F., and Warnatz, J., *Catalysis Today* 21:461–470 (1994).
5. Deutschmann, O., Schmidt, R., Behrendt, F., and Warnatz, J., *Proc. Combustion Institute* 26:1747–1754 (1996).
6. Hickman, D. A., and Schmidt, L. D., *AIChE* 39, 7:1164–1177 (1993).
7. Hellsing, B., Kasemo, B., and Zhdanov, V. P., *J. Catalysis* 132:210–228 (1991).
8. Fridell, E., Rosen, A., and Kasemo, B., *Langmuir* 10:699–708 (1994).
9. Rinnemo, M., Kulginov, D., Johansson, S., Wong, K. L., Zhdanov, V. P., and Kasemo, B. *Surface Science* 376:297–309 (1997).
10. Aghalayam, P., Park, Y. K., and Vlachos, D. G., *Proc. Combustion Institute* 28:1331–1339 (2000).
11. Dogwiler, U., Benz, P., and Mantzaras, J., *Combust. Flame* 116:243– 258 (1999).
12. Dogwiler, U., Mantzaras, J., Benz, P., Kaeppeli, B., Bombach, R., and Arnold, A., *Proc. Combustion Institute* 27:2275–2282 (1998).
13. Deutschmann, O., and Schmidt, L. D., *AIChE* 44, 11:2465–2477 (1998).
14. Mantzaras, J., and Benz, P., *Combust. Flame* 119:455–472 (1999).
15. Mantzaras, J., Appel, C., and Benz, P., *Proc. Combustion Institute* 28:1349–1357 (2000).
16. Dobbeling, K., and Griffin, T., patent No. US5937632, 1999.
17. Pfefferle, W. C., and Pfefferle, L. D., *Progress Energy and Combust. Sci.* 12:25–41 (1985).
18. Bui, P. A., Vlachos, D. G., and Westmoreland, P. R., *Proc. Combustion Institute* 26:1763–1770 (1996).
19. Warnatz, J., Dibble, R. W. and Maas, U., *Combustion, Physical and Chemical Fundamentals, Modeling and Simulation*, Springer-Verlag, New York, 1996.
20. GRI-3.0, Gas Research Institute, http://www.me.berkeley.edu/gri_mech, 1999.
21. Mueller, M. A., Kim, T. J., Yetter, R. A., and Dryer, F. L., *Int. J. Chemical Kinetics* 31:113–125 (1999).
22. Miller, J. A., and Bowman, C. T., *Prog. Energy Combust. Sci.* 15:287–338 (1989).

23. Ikeda, H., Libby, P. A., Williams, F. A., and Sato J., *Combust. Flame* 93:138–148 (1993).
24. Schefer, R. W., *Combust. Flame* 45:171–190 (1982).
25. Markatou, P., Pfefferle, L. D., and Smooke, M. D., *Combust. Sci. Technol.* 79:247–268 (1991).
26. Buser, S., Benz, P., Schlegel, A., and Bockhorn, H., *Ber. Bunsenges. Phys. Chem.* 97(12):1719–1723 (1993).
27. Mantzaras, J., Appel, C., Benz, P., and Dogwiler, U., *Catalysis Today* 59:3–17 (2000).
28. Deutschmann, O., Maier, L. I., Riedel, U., Stroemman, A. H., and Dibble, R. W., *Catalysis Today* 59:141–150 (2000).
29. Arnold, A., Bombach, R., Kaeppeli, B., and Schlegel, A., *Appl. Physics B*, 64:579–583 (1997).
30. Brockhinke, A., Andresen, P., and Kohse-Höinghaus, K., *Appl. Physics B*, 61:533–545 (1995).
31. Eisenberg, S., "Raman Spektroskopie an einer Zerstäuberflamme", Diploma Thesis, Max-Planck-Institut für Strömungsforschung, Göttingen (1995).
32. Williams, F. A., *Combustion Theory*, Second Edition, Benjamin/Cummings, Menlo Park, CA., 1985, p. 633.
33. Kee, R. J., Dixon-Lewis, G., Warnatz, J., Coltrin, M. E., and Miller, J. A., "A Fortran computer code package for the evaluation of gas-phase multicomponent transport properties", Sandia report SAND86–8246, July 1996 reprint.
34. Patankar, S., *Numerical Heat Transfer and Fluid Flow*, Hemisphere, New York, 1980, p. 131.
35. Srivatsa, S. K., "Cham computer code 201, CORA2—A Computer code for axisymmetrical combustion chambers", CHAM TR 201/1, 1977.
36. Kuijlaars, K. J., Kleijn, C. R., and van den Akker, H. E. A., *Chemical Engineering J.* 57:127–136 (1995).
37. Raja, L. L., Kee, R. J., Deutschmann, O., Warnatz, J., and Schmidt, L. D., *Catalysis Today* 59:47–60 (2000).
38. Kee, R. J., Rupley, F. M., and Miller, J. A., "The CHEMKIN thermodynamic data base", Sandia report SAND87–8215B, July 1996 reprint.
39. Hills, A. J., and Howard, C. J., *Chem. Physics* 81(10): 4458–4465 (1984).
40. Warnatz, J., Allendorf, M. D., Kee, R. J., and Coltrin, M. E., *Combust. Flame* 96:393–406 (1994).
41. Kee, R. J., Rupley, F. M., and Miller, J. A., "CHEMKIN II: A Fortran chemical kinetics package for the analysis of gas-phase chemical kinetics", Sandia report SAND89–8009B, July 1996 reprint.
42. Coltrin, M. E., Kee, R. J., and Rupley, F. M., "Surface CHEMKIN A Fortran package for analyzing heterogeneous chemical kinetics at the solid surface-gas phase interface", Sandia report SAND90–8003C, July 1996 reprint.
43. Lutz, A. E., Kee, R. J., and Miller, J. A., "SENKIN: A fortran program for predicting homogeneous gas phase chemical kinetics with sensitivity analysis", Sandia report SAND87–8248, July 1996 reprint.
44. Bengtsson, K. U. M., Benz, P., Schaeren, R., and Frouzakis, C., *Proc. Combustion Institute* 27:1393–1399 (1998).
45. Hellsing, B., Kasemo, B., Ljungström, S., Rosen, A., and Wahnström, T., *Surface Sci.* 189/190:851–860 (1987).
46. Williams, W. R., Marks, C. M., and Schmidt, L. D., *J. Phys. Chemistry* 96:5922–5931 (1992).
47. Fassihi, M., "Catalytic oxidation of H_2 on Pt", Doctoral Thesis, Chalmers University of Technology, Department of Physics, Goeteborg, 1991, pp. 47–48.
48. Law, C. K., and Sivashinsky, G. I. *Combust. Sci. Technol.* 29:277–286 (1982).

Received 17 April 2001; revised 25 October 2001; accepted 7 November 2001